# Similarity scaling and vorticity structure in high-Reynolds-number stably stratified turbulent wakes

PETER J. DIAMESSIS[1]†, GEOFFREY R. SPEDDING[2]
AND J. ANDRZEJ DOMARADZKI[2]

[1]School of Civil and Environmental Engineering, Cornell University, Ithaca, NY 14853, USA

[2]Department of Aerospace and Mechanical Engineering, University of Southern California, Los Angeles, CA 90089-1191, USA

The mean velocity profile scaling and the vorticity structure of a stably stratified, initially turbulent wake of a towed sphere are studied numerically using a high-accuracy spectral multi-domain penalty method model. A detailed initialization procedure allows a smooth, minimum-transient transition into the non-equilibrium (NEQ) regime of wake evolution. A broad range of Reynolds numbers, $Re = UD/\nu \in [5 \times 10^3, 10^5]$ and internal Froude numbers, $Fr = 2U/(ND) \in [4, 64]$ ($U$, $D$ are characteristic velocity and length scales, and $N$ is the buoyancy frequency) is examined. The maximum value of $Re$ and the range of $Fr$ values considered allow extrapolation of the results to geophysical and naval applications.

At higher $Re$, the NEQ regime, where three-dimensional turbulence adjusts towards a quasi-two-dimensional, buoyancy-dominated flow, lasts significantly longer than at lower $Re$. At $Re = 5 \times 10^3$, vertical fluid motions are rapidly suppressed, but at $Re = 10^5$, secondary Kelvin–Helmholtz instabilities and ensuing turbulence are clearly observed up to $Nt \approx 100$. The secondary motions intensify with increasing stratification strength and have significant vertical kinetic energy.

These results agree with existing scaling of buoyancy-driven shear on $Re/Fr^2$ and suggest that, in the field, the NEQ regime may last up to $Nt \approx 1000$. At a given high $Re$ value, during the NEQ regime, the scale separation between Ozmidov and Kolmogorov scale is independent of $Fr$. This first systematic numerical investigation of stratified turbulence (as defined by Lilly, *J. Atmos. Sci.* vol. 40, 1983, p. 749), in a controlled localized flow with turbulent initial conditions suggests that a reconsideration of the commonly perceived life cycle of a stratified turbulent event may be in order for the correct turbulence parametrizations of such flows in both geophysical and operational contexts.

**Key words:** ocean processes, stratified flows, turbulence simulation

## 1. Introduction

### 1.1. *The importance of stably stratified wakes*

Stably stratified turbulent wakes are fundamental fluid flows of relevance to environmental and ocean engineering applications. Geophysical examples include

† Email address for correspondence: pjd38@cornell.edu

the oceanic wakes of islands (Tomczak 1988), headlands (Pawlak *et al.* 2003) and seamounts (Gibson, Nabatov & Ozmidov 1993) and the atmospheric wakes of mountains (Rotunno, Grubisic & Smolarkiewicz 1999). Such wakes are potent agents of across and along-isopycnal transport and mixing of energy, heat and biogeochemical constituents not only near the wake source but also over significant distances away from it. From an ocean engineering perspective, underwater vehicles operate most efficiently in the pycnocline of the open or littoral ocean. The ambient stratification, however, has a unique effect on the vehicle wake through the formation of distinct late-time, large aspect ratio quasi-horizontal vortices (commonly known as 'pancakes') (Lin & Pao 1979) and the radiation of internal waves both by the vehicle and its turbulent wake. Thus, the wake may establish a distinct late-time signature that may potentially be traced directly to the generating body. Finally, a turbulent wake in a stably stratified fluid serves as an efficient template for examining the fundamental physics of a localized turbulent event under the competing influences of background shear and ambient stable stratification (Thorpe 2005).

## 1.2. *The towed sphere stratified wake*

### 1.2.1. *Laboratory experiments*

Motivated by its inherent simplicity, the wake of a sphere towed in a uniform stratification has emerged as a convenient prototype to investigate the structure and dynamics of stratified turbulent wakes. A review of research on stably stratified wakes of a variety of bluff bodies (including momentumless self-propelled body wakes) prior to 1980 may be found in the article by Lin & Pao (1979). A significant body of work on the dynamics of stratified towed-sphere wakes has considered the near wake (Lin *et al.* 1992; Chomaz, Bonetton & Hopfinger 1993*b*), the generation of lee-waves and wake-emitted internal waves (Bonneton, Chomaz & Hopfinger 1993) and vertical diffusion in the late wake (Chomaz *et al.* 1993*a*).

Systematic quantitative investigations of the stratified turbulent wake of a towed sphere were performed by Spedding and co-workers (Spedding, Browand & Fincham 1996*b*; Spedding 1997, 2001, 2002, hereafter referred to as SBF96b, Sp97, Sp01 and Sp02, respectively). Particle image velocimetry (PIV) was used to obtain accurate two-dimensional measurements of the velocity field across horizontal and vertical transects through the mid-to-late time wake. A broad range of internal Froude numbers, $Fr \equiv 2U/(ND) \in [4, 240]$, was considered, where $U$, $D$ and $N$ are the tow speed, sphere diameter and stratification frequency, respectively. The maximum body-based Reynolds number, $Re = UD/\nu$, value attained in these experiments was $Re = 2 \times 10^4$. For a minimum value of $Re \approx 5 \times 10^3$, scaling arguments (Spedding, Browand & Fincham 1996*a*) and subsequent experiments (SBF96b) found that the minimum Froude number value necessary to obtain a fully three-dimensional turbulent near wake was equal to $Fr \approx 4$, in agreement with the value proposed by Chomaz *et al.* (1993*b*). For the above $Fr$ range and values of $Re$ exceeding the indicated minimum, Sp97 demonstrated that all wakes have similar scaling behaviour. The underlying cause for the similar scaling is that the decrease in local wake velocities is accompanied by an increase in local length scales. As a result, a local Froude number based on these scales will decrease until it becomes $O(1)$. Thus, the late stages of even a weakly stratified wake will eventually be fully controlled by buoyancy.

On the basis of observations of the temporal variation of the exponents of the power laws associated with the self-similar scaling of the mean defect velocity profile, Sp97

identified three dynamical regimes in stratified wake evolution. At early times, three-dimensional (3D) non-stratified turbulent axisymmetric wake structure and dynamics govern the flow. The maximum defect velocity $U_0$ decays with a $U_0 \sim (Nt)^{-2/3}$ law, whereas both the Gaussian half-width and height of the mean defect profile follow an $(Nt)^{1/3}$ growth rate. Experiments (Browand, Guyomar & Yoon 1987), numerical simulations (Itsweire *et al.* 1993) and theoretical analyses (Gibson 1980; Riley & Lelong 2000) of decaying stratified turbulent flows conducted prior to Sp97 indicate that buoyancy forces begin to influence the larger scales of the flow at $Nt \approx 1$. The corresponding manifestation of the onset of buoyancy control in experiments on stratified wakes of self-propelled slender bodies was a suspension of the growth of the wake height at $Nt = 2$ (Lin & Pao 1979).

At $Nt \approx 2$, the wake dynamics transition into the non-equilibrium (NEQ) regime which is characterized by reduced decay rates of the horizontal mean velocity, with $U_0 \sim (Nt)^{-0.25}$. The laboratory investigations of Bonnier & Eiff (2002) also report an increase in the defect velocity over the interval $2 \leqslant Nt \leqslant 7$. Sp97 conjectured that this deceleration of mean defect velocity decay can be attributed to the conversion of available potential to kinetic energy near the wake centre through re-stratification effects. The wake width continues to grow with an $(Nt)^{1/3} \sim (x/D)^{1/3}$ power law (SBF96b; Sp97), exactly like its unstratified counterpart (Tennekes & Lumley 1972). In contrast, the wake height remains approximately constant throughout NEQ and was found to scale approximately with an empirically obtained $Fr^{0.6}$ (Sp02). Two other key features of NEQ are the gradual suppression of vertical velocities and transport inside the wake core (Sp01) and the radiation of high-frequency internal waves from the wake into the ambient. It is during the NEQ regime that coherent patches of vertical vorticity (hereafter referred to as 'pancake' vortices) emerge, enlarging both by merging and diffusion (Sp97).

A steeper decay rate of the mean defect velocity, with $U_0 \sim (Nt)^{-0.76}$, is observed at a transition time of $Nt \approx 50$, leading into the quasi-two-dimensional regime (Q2D) that persists for all measurable times up to $Nt \approx 2000$ (Sp97). The $(Nt)^{1/3}$ power law continues to characterize wake-width growth. The wake height transitions into a diffusively driven growth. Once the Q2D regime has been established, almost all remaining kinetic energy in the flow resides within the field pancake vortices, as vertical velocities are near-negligible. The flow field nonetheless is not purely two-dimensional and the mean flow does not follow the decay laws of a two-dimensional wake (Tennekes & Lumley 1972). Significant variability is observed in the vertical. Vorticity fields indicate pairs of opposite-signed stable and highly diffuse inclined vertical shear layers (Sp02). Each shear layer pair is inferred to be a cross-section through a vertically coherent pancake eddy, with the maximum shear occurring at the pancake edges. Viscous diffusion provides a means of vertical coupling across shear layers and is responsible for their thickening and eventual merging. Eventually, the vertical centreplane flow field is dominated by the mean wake defect, as indicated by the establishment of two almost-horizontal layers of opposite-signed vorticity.

### 1.2.2. *Numerical simulations*

The direct numerical simulations (DNS) of Gourlay *et al.* (2001) and large-eddy simulations (LES) of Dommermuth *et al.* (2002), run at maximum Reynolds numbers of $Re = 10^4$ and $Re = 10^5$, respectively, have also replicated the basic phenomenology of the NEQ and Q2D regimes. However, the lack of agreement in vertical wake length scale growth rates between experiments is also present in the numerical studies.

Although both numerical investigations show a constant wake height upon the onset of the NEQ regime, the scaling of the height as a function of $Fr$ was never resolved as each set of simulations was run for only a finite value of $Fr$. Specifically, Gourlay *et al.* (2001) and Dommermuth *et al.* (2002) consider values of $Fr = 10$ and $Fr = 4$, respectively.

To minimize computational complexity, neither of the above studies employs a sphere in the simulation. Their initial condition is an approximation to the near wake. In both cases, pancake eddies emerge in the late wake despite the absence of the sphere or any externally imposed coherent structure on the initial condition. Three-dimensional visualizations of the vorticity field by Gourlay *et al.* (2001) reveal pancake eddies with a geometry similar to that of isolated vortex dipoles generated in laboratory experiments (Praud & Fincham 2005). Gourlay *et al.* (2001) do not observe multiple layers of pancake eddies connected by the complex vortex line configuration conjectured by Spedding (2002). However, such an observation may be biased by the relatively low values of $Fr$ and $Re$ (Billant & Chomaz 2001; Sp02). The vorticity visualizations of Dommermuth *et al.* (2002) focus on horizontal transects of vertical vorticity. When their $Re$ is increased by a factor of $10$–$10^5$, an enhanced fine structure is observed until $Nt \approx 40$. Diffuse pancake vortices (like those reported in low-$Re$ laboratory experiments) then emerge as soon as $Nt \approx 50$. Dommermuth *et al.* (2002) do not show any vertical cuts of the spanwise vorticity field.

The very recent DNS study of Brucker & Sarkar (2010) has focused on contrasting the mean flow scaling and the energy budgets between non-zero momentum and momentumless wakes at $Re = 10^4$ and $5 \times 10^4$ and $Fr = \infty$ and 4. Values of $Fr = 2$ and 20 are considered at $Re = 10^4$ for the non-zero momentum case but are used strictly for comparison with previous experimental and computational studies. In terms of the non-zero momentum case, this investigation agrees overall with the findings of Gourlay *et al.* (2001) and Dommermuth *et al.* (2002) on the mean flow scaling but does not provide results on the vorticity structure of the flow. In agreement with Diamessis & Spedding (2006), a prolonged duration of the NEQ regime at $Re = 5 \times 10^4$ is reported. Furthermore, the decay law of the turbulent kinetic energy dissipation rate is found to follow inertial range scaling (Tennekes & Lumley 1972).

### 1.2.3. *Self-similarity analysis*

In an attempt to replicate the scaling behaviour of laboratory wakes and establish a predictive tool for wake scaling at $Re$ relevant to geophysical and ocean engineering flows, Meunier, Diamessis & Spedding (2006) employ self-similarity analysis to develop a scaling model for the mean flow evolution of a stratified turbulent wake. The model assumes a self-similarly evolving near wake for which all vertical velocities and Reynolds stresses are zero for $Nt \geqslant 2$. Beyond $Nt = 2$, the mean wake dynamics are governed by a balance between turbulent diffusion of momentum in the horizontal and strictly viscous diffusion of momentum in the vertical. A laminar, purely viscously driven wake is finally established at very large distances ($x/D \approx O(Re^3)$) from the body. Overall, when compared with corresponding mean flow measures from the laboratory and DNS/LES, the model shows good agreement in terms of power-law exponents and transition points between regimes of evolution. A notable exception is that the model diverges from the experimentally observed 1/3 power-law exponent for the wake width which exhibits an $(Nt)^{1/2}$ and $(Nt)^{1/4}$ growth in the NEQ and Q2D regimes, respectively.

### 1.3. *High-Reynolds-number turbulence in strong stratification*

Motivated by the observations of Lin & Pao (1979), Lilly (1983) proposed a modification at high $Re$ to the intermediate-to-late time phase of the life cycle of a localized turbulent event evolving in an ambient stratification, as discussed in §1.2.1. He conjectured that, with increasing $Re$, the vertical shear layers will become thinner, leading to a loss of vertical coherence. As the layers thin, the local conditions for Kelvin–Helmholtz instabilities will become more favourable, leading to the formation of secondary instabilities and turbulence and the establishment of a horizontal energy spectrum with a $-5/3$ slope spanning a broad range of motions (this spectral signature was proposed as the result of an inverse energy cascade process). Lilly (1983) regards this state of motion as 'stratified turbulence' and this term is used throughout this paper to refer to the secondary instabilities and turbulence induced by buoyancy-driven shear. Lilly's hypothesis has been corroborated by Riley & de Bruyn Kops (2003) (hereafter referred to as RdBK), whose DNS employs an initial condition consisting of a periodic array of oppositely signed Taylor–Green vortices that gradually destabilize into pancake vortices. For values of $Re_l$ in the range of $[800, 6400]$, where $l$ is a numerically imposed initial length scale of the Taylor–Green vortices, the large scales show a weak dependence on $Re_l$, a finding consistent with the observations of Dommermuth *et al.* (2002). However, at sufficiently high $Re_l$, intermittent secondary Kelvin–Helmholtz instabilities develop, which lead to localized patches of secondary turbulence (Hebert & de Bruyn Kops 2006) with elevated levels of vertical kinetic energy.

Similar secondary instabilities and turbulence have been observed in DNS of stratified homogeneous turbulence with and without rotation (Waite & Bartello 2003; Brethouwer *et al.* 2007), DNS of an idealized late wake, consisting of an array of staggered pancake vortices (Winters, McKinnon & Mills 2004), and DNS of a pair of counter-rotating vertical vortices destabilized via zigzag instability in a stratified fluid (Deloncle, Billant & Chomaz 2008). Finally, DNS of forced strongly stratified homogeneous turbulence, where the values of $N$ and $\nu$ were gradually adjusted to allow for a near constant value of turbulent Froude number of 0.08 and a progressive increase of a Taylor-microscale based Reynolds number from 200 to 1000, reported the emergence of overturning motions over roughly 1 % of the volume of the computational domain when this Reynolds number exceeds the value of 700 (Laval, McWilliams & Dubrulle 2003).

The findings of the studies discussed above suggest that stratified wake flows should be examined more closely. The end result could be important because the instabilities and subsequent turbulence have the potential to significantly modify the flow evolution at high Reynolds number, which is, in fact, representative of most practical applications. Isolated observations of Kelvin–Helmholtz-like billows at times as late as $Nt \approx 70$ and 90 in towed grid (Fincham, Maxworthy & Spedding 1996) and wake experiments (Sp02) provide preliminary evidence for the importance of these secondary events in high-$Re$ wake flows. However, no systematic investigation exists in current literature of such secondary motions in a *localized* canonical stratified flow with *turbulent* initial conditions, e.g. a wake or jet.

### 1.4. *Objectives and basic questions*

The primary objective of this study is to investigate the scaling and flow structure of a stratified turbulent wake over as broad a range of $Re$ and $Fr$ values as possible, thereby extending beyond the corresponding restrictions of previous experiments

and numerical simulations. To achieve this objective, a parallel spectral multi-domain penalty method flow solver (Diamessis, Domaradzki & Hesthaven 2005, hereafter referred to as DDH) is employed which is stabilized by explicit spectral filtering. The high accuracy (due to its lower truncation error as compared to finite-difference, finite-element and finite-volume schemes), spatial adaptivity and explicitly controlled (via spectral filtering) artificial dissipation of this solver equip it with unique advantages over equivalent numerical tools employed in past numerical studies. As a result, the reproduction of the vertical structure of the wake throughout its entire evolution is enabled at very high accuracy and resolution, unavailable to previous numerical investigations, without concerns of spurious smoothing of the scales critical to the dynamics of secondary motions. The intrinsic sensitivity of a spectral/spectral-multi-domain scheme to any assumptions on initial/boundary conditions and forcing (Boyd 2001) has also led to a much more rigorous and careful treatment of simulation initialization than that previously given in the literature.

This study aims to build on preliminary results by Diamessis & Spedding (2006) and is driven by the following fundamental questions: What is the effect of $Re$ on the $Fr$-based scaling of the mean wake flow and the transition times across different dynamical regimes as observed by Sp97 and Sp02? At high $Re$, will spectral multi-domain-based LES (with its inherently weak artificial dissipation and strong localized resolution of the wake core) reproduce secondary Kelvin–Helmhotz instabilities and turbulence in the intermediate-to-late time wake? If indeed such secondary instabilities are established, do they inhibit or simply delay the formation of pancake vortices? Finally, how realistic are the assumptions of Meunier *et al.* (2006) of negligible vertical transport at $Nt \geqslant 2$ at high $Re$?

## 2. Model formulation

### 2.1. *Problem geometry*

The base flow considered in this investigation is a stratified turbulent wake with non-zero net momentum. Such a flow corresponds to the mid-to-late time wake of a radially symmetric object of characteristic length scale $D$ towed at velocity $U$ in a linear density stratification of frequency $N$, where

$$N^2 \equiv -\frac{g}{\rho_0} \frac{\mathrm{d}\overline{\rho}}{\mathrm{d}z}, \qquad (2.1)$$

where, according to the Boussinesq approximation, $\rho_0$ is a reference density and $\overline{\rho}_{(z)}$ is the departure of the background density profile from this reference value. For the purposes of this study, the radially symmetric object is considered to be a sphere to allow comparison with relevant laboratory investigations (SBF96b; Sp97; Sp02). Challenges of computational complexity (elaborated upon further in §3) prevent the spatial discretization from accounting for the sphere and keep its focus only on the flow generated in the sphere's wake. Thus, as implemented by Orszag & Pao (1975) and in more recent studies of stratified turbulent wakes (Gourlay *et al.* 2001; Dommermuth *et al.* 2002; Diamessis *et al.* 2005; Brucker & Sarkar 2010), the computational domain and spatial discretization do not account for the sphere and focus only on the flow generated in its wake. Specifically, the computational domain is a three-dimensional volume inside the wake region, centred on the wake centreline. Within this volume of dimensions $L_x \times L_y \times L_z$ (shown in figure 1), the three-dimensional and time-dependent wake flow field is computed. Effectively, the
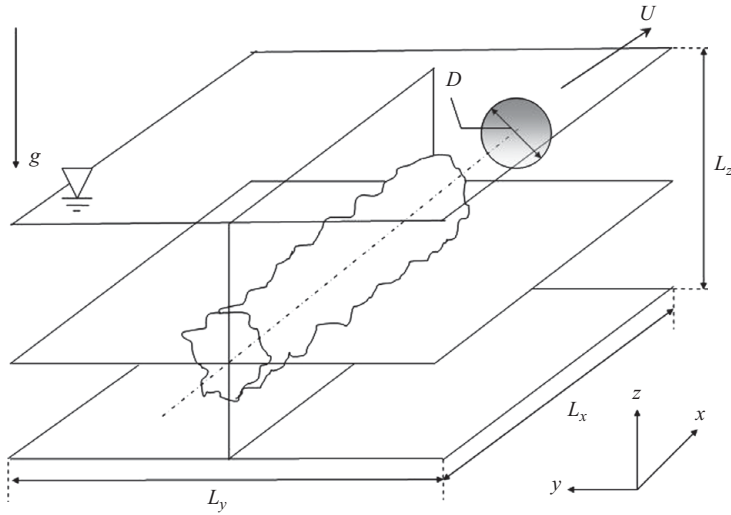
FIGURE 1. Computational domain for the simulation of a mid-to-late-time stratified turbulent wake with non-zero net momentum. The wake was originally generated by a sphere of diameter $D$, towed with a velocity $U$, which however is not present in the computational domain. The domain dimensions are $L_x \times L_y \times L_z$. Consistent with the salt-stratified water tank, the domain has a solid wall bottom and free-slip top.

computational domain may be regarded as an approximation to a three-dimensional 'window' fixed in a stratified water tank, similar to the PIV sampling windows of SBF96b and Sp02.

In this fixed reference frame, the sphere is assumed to have travelled through the domain as it continues to move from left to right. After evolution time $t$, the results may be interpreted as a realization of the above computation volume at a distance $x = x(U/t) = x_0 + Ut$ behind the moving sphere, where $x_0 = 8D$ (see also § 3.2).

The numerically computed solution is statistically homogeneous along the wake axis but is non-stationary in time. The wake in the frame of a uniformly moving sphere is statistically stationary in time but inhomogeneous in the direction of the wake axis. We refer the interested reader to Orszag & Pao (1975) and Dommermuth *et al.* (2002) on how the above Galilean transformation between $x$ and $t$ directly relates streamwise spatial averages in our numerical solution to time averages computed behind a uniformly translating sphere.

The domain is assumed to be periodic in both horizontal directions. The periodicity assumption in the $x$-direction is valid because the length of the computational domain is much smaller than the total wake length (Dommermuth *et al.* 2002), which ensures that the streamwise variation of all average quantities is negligible compared with their variation in the spanwise and vertical directions. The spanwise periodicity assumption is valid provided the horizontal length scale of the wake does not exceed a threshold value, beyond which interactions with the wake's spanwise-periodic image are possible. Although a laboratory-fixed reference frame is considered, streamwise periodicity allows a temporally evolving simulation which can be run up to as late as $Nt \approx O(2000)$ (Dommermuth *et al.* 2002). Because of spanwise periodicity, internal waves radiated by the wake re-enter the computational domain and thus after a certain point later in time, the internal wave field does not correspond to its experimental

counterpart. However, by that time the flow is efficiently decomposed into internal waves and quasi-two-dimensional vortical modes and analysis of the latter (Riley & Lelong 2000) is possible in isolation.

## 2.2. *Governing equations and boundary conditions*

The equations governing the problem investigated are the incompressible Navier–Stokes equations under the Boussinesq approximation (DDH):

$$\frac{\partial \boldsymbol{u}}{\partial t} = -\frac{1}{2}[\boldsymbol{u}\cdot\nabla\boldsymbol{u} + \nabla(\boldsymbol{u}\cdot\boldsymbol{u})] + \boldsymbol{F}_g - \frac{1}{\rho_0}\nabla p' + \nu\nabla^2\boldsymbol{u}, \qquad (2.2)$$

$$\frac{\partial \rho'}{\partial t} = -\nabla\cdot(\boldsymbol{u}(\rho' + \overline{\rho}(z))) + \kappa\nabla^2\rho', \qquad (2.3)$$

$$\nabla\cdot\boldsymbol{u} = 0, \qquad (2.4)$$

where

$$\boldsymbol{F}_g = -g\frac{\rho'}{\rho_0}\hat{\boldsymbol{k}}, \qquad (2.5)$$

$\boldsymbol{u} = (u, v, w)$ is the velocity vector and $\boldsymbol{k}$ is the normal unit vector in the vertical direction. The nonlinear term in (2.2) is written in the skew-symmetric form to minimize aliasing effects in the numerical solution (Boyd 2001). The quantities $p'$ and $\rho'$ are the perturbations of the pressure and the density from their respective (mean) reference values, which are in hydrostatic balance (DDH).

The boundary conditions used in the numerical model correspond to the description of the computational domain given in §2.1. In the horizontal direction, periodic boundary conditions are employed. The bottom boundary is a solid wall with a no-slip boundary condition. The top boundary is a free-slip non-deformable surface. Finally, the density perturbation is subject to a Dirichlet boundary condition at both vertical boundaries.

## 2.3. *Numerical method*

The temporal discretization of (2.2) and (2.4) consists of three fractional steps (DDH): the explicit treatment of the nonlinear terms, the implicit solution of a Poisson equation for the pseudo-pressure, which ensures an incompressible velocity field, and the implicit solution of a Helmholtz equation for the viscous terms, where the physical boundary conditions are imposed. This splitting approach combines third-order stiffly stable and backward-differentiation schemes with a dynamic high-order boundary condition for the pressure. Thus, the maximum possible value of stable time step is attainable (Karniadakis, Israeli & Orszag 1991). An analogous operator-splitting approach is used for the advection-diffusion equation (2.3) for the density. Finally, an adaptive time-stepping scheme is employed to smoothly increase the time step during the less energetic buoyancy-dominated regime of the flow evolution, thereby minimizing the cost of advancing the simulations as far as possible in time. Conversely, at higher $Re$, where the emergence of secondary energetic instabilities is likely at intermediate times, adaptive time stepping enables an automatic decrease of the time step. Through application to canonical test cases such as the primary instability of a temporally evolving shear layer and fully developed laminar channel flow, the solver has been tested over a range of step sizes spanning two orders of magnitude and has been found to be $O(\Delta t^2)$.

In the periodic horizontal direction, Fourier spectral discretization is used with $\hat{N}_x$ and $\hat{N}_y$ Fourier modes in the longitudinal and spanwise directions, respectively. In the vertical direction, the computational domain is partitioned into $M$ subdomains of variable height $H_k$ ($k = 1, \ldots, M$) and fixed order of polynomial approximation $\hat{N}$ (figure 3). The total number of vertical grid points is $\hat{N}_z = M(\hat{N}+1)+1$. Within each subdomain, a Legendre spectral collocation scheme (Boyd 2001) is used. Subdomains communicate with their neighbours via a simple patching condition (DDH). The multi-domain scheme allows for increased vertical resolution in the turbulent core of the wake while also resolving adequately, yet not excessively, the internal wave-dominated ambient.

The resolutions used in this paper aim to capture the dynamically relevant scales of motion in the wake while accommodating available computational resources and the need for rapid run turnaround. As a result, the available numerical resolution at higher Reynolds numbers is not sufficient to capture both the large, energy-containing and small, dissipative scales of turbulence. With the bulk of the numerical resolution devoted to large scales, the effects of molecular viscosity which are active in the range of small, dissipative scales cannot be resolved. Attempts to solve Navier–Stokes equations using DNS in such a case will result in an under-resolved simulation. When spectral schemes, which are inherently non-dissipative, are used in under-resolved simulations, the resulting Gibbs oscillations are compounded by aliasing effects driven by the nonlinear term, leading to catastrophic numerical instabilities (Gottlieb & Hesthaven 2001). To overcome such difficulties, either the governing equations must be modified, e.g. by introducing an explicit subgrid-scale (SGS) model term as is commonly done in LES, or by modifying the numerical method of solution by introducing procedures that control and prevent numerical instabilities. We follow the latter approach using two techniques that are designed to ensure stability of the numerical solution while preserving high accuracy: explicit spectral filtering and penalty schemes (see §2.4 for a summary and DDH for details).

All simulations were performed using a parallel version of the Navier–Stokes solver based on the single process multiple domain (SPMD) paradigm. In physical space, the computational domain is partitioned along the spanwise direction into distinct vertical slabs of thickness $L_y/\hat{N}_P$ and each slab is assigned to one of $\hat{N}_P$ processors. Communication across processors is implemented through the message passing interface (MPI). In Fourier space, the computational domain is partitioned into vertical slabs of thickness $L_x/\hat{N}_P$.

### 2.4. *Stabilization methods: spectral filtering and penalty techniques*

Penalty methods consist of collocating a linear combination of the equation and boundary/patching conditions (the latter multiplied by a penalty coefficient) at the boundaries/subdomain interfaces, respectively (Hesthaven & Gottlieb 1996; Hesthaven 1997). A smooth transition from the subdomain interface to its interior is thus possible, enabling stable computation of the high-*Re* 'internal' (internal with respect to the subdomain boundary) dynamics of the flow without having to resolve the thin numerical/viscous physical boundary layers or internal sharp gradients at subdomain interfaces (DDH).

Spectral filtering consists of the explicit application of an order $p$ low-pass filter function to the spectral (modal) expansion of the solution. Application of a $p$th order spectral filter is the non-stiff equivalent to the use of a $p$th order hyperviscous operator in the governing equations (Gottlieb & Hesthaven 2001).

In this study, an exponential filter (Gottlieb & Hesthaven 2001) is used:

$$\sigma(k) = \exp\left[-\alpha\left(\frac{k}{k_c}\right)^p\right], \tag{2.6}$$

where $p$ is the filter order and $\alpha = -\ln(\varepsilon_M)$, with $\varepsilon_M$ being the machine precision. In Legendre space, the filter function $\sigma(k)$ multiplies the $k$th Legendre modal coefficient and $k_c$ represents the index of the highest resolved mode. In contrast, in Fourier space, for the purpose of implementing efficient two-dimensional filtering, $k$ is selected to represent the magnitude of an individual Fourier wavenumber pair $(k_x, k_y)$, i.e. $k = (k_x^2 + k_y^2)^{1/2}$ and $k_c$ is chosen as $k_c \equiv [(k_{x,max}^2 + k_{y,max}^2)]^{1/2}$, i.e. the maximum resolved Fourier wavenumber pair magnitude for the given domain dimensions.

In terms of the temporal discretization summarized in §2.3, the penalty method is applied at two different levels (explicit advancement of nonlinear terms and implicit treatment of viscous terms) in the incompressible Navier–Stokes equations. Legendre spectral filtering of the same order $p$ is applied after all three fractional steps. Fourier spectral filtering is applied only after advancing the nonlinear terms to suppress the accumulation of high-wavenumber numerical noise driven by aliasing.

Legendre filters have a negligible influence on the subdomain interfaces (Gottlieb & Hesthaven 2001), where the influence of the penalty method is the strongest. Thus, the two stabilizing techniques complement each other in enabling numerical stability through the entire extent of a spectral subdomain. As a final safeguard against numerical instability, adaptive interfacial averaging is used in the vertical direction (DDH).

## 2.5. *Relation of spectral filtering to LES*

LES techniques are used in situations where available numerical resolution is insufficient to simulate all dynamically relevant scales of turbulence. The classical LES approach uses physical arguments to account for the effects of small scales that cannot be resolved on an LES mesh. Most frequently, these effects are represented through an eddy viscosity term that intends to model an energy flux to the unresolved scales as the turbulence-enhanced dissipation. Another approach, initially proposed by Boris *et al.* (1992), and often regarded as implicit large-eddy simulation (ILES), is based on the observation that truncation errors in certain discretizations of Navier–Stokes equations introduce numerical dissipation with the implicit effects of the discretization qualitatively similar to the effects of the explicit SGS models in traditional LES. Specifically, such behaviour is observed if one discretizes the Navier–Stokes equations (2.2)–(2.4) using higher-order non-oscillatory methods, also known as monotonicity or shape preserving, shock capturing or monotone schemes; e.g. total variation diminishing (TVD), flux-corrected-transport (FCT) and various flux-limited and sign-preserving schemes (Zalesak 1979; Sweby 1984; Harten *et al.* 1987). A good review of ILES and its applications is given by Grinstein & Fureby (2002) and in a recent book by Grinstein, Margolin & Rider (2007).

More broadly, ILES can be defined as any procedure for under-resolved simulations of turbulence that relies on purely numerical techniques to achieve stable simulations. Sometimes such methods are called stabilized LES (Minguez, Pasquetti & Serre 2009). In that sense, the simulations presented herein may be viewed as a spectral implicit LES where the stabilization is not provided by the truncation error of the numerical discretization (which is exponentially small for a spectral method, Boyd 2001) but by the spectral filter, which may be viewed as an

intrinsic component of the numerical discretization in the case of under-resolved simulations.

When using ILES one must, of course, be aware that simply guaranteeing numerical stability does not guarantee physically correct dynamics of the resolved scales. Therefore, the results from ILES must always be compared with experiments and simulations, either fully resolved DNS, or LES performed with other models, to gain confidence that the method is not only numerically stable but also physically correct. To this end, implicit LES of various flows that combine high-accuracy spatial discretizations with explicit filtering have shown very good agreement with measurements, previous DNS and theory in terms of large-scale quantities (e.g. decay rates of turbulent kinetic energy, profiles of mean and r.m.s. (root mean square) fluctuating velocity and Reynolds stresses, and energy spectra) (Bogey & Bailly 2006; Sengupta, Jacobs & Mashayek 2009). In a similar context, the spectral vanishing viscosity (SSV) method, frequently used with spectral techniques, has been validated e.g. by Karamanos & Karniadakis (2000) and Minguez *et al.* (2009). Furthermore, for compressible flows, Cook & Cabot (2005) applied hyperviscosity to shear–turbulence interaction to achieve spectral-like behaviour.

Such methods may be particularly suitable for the simulation of stratified flows where the assumptions of isotropy and homogeneity, a fundamental building block of many eddy viscosity-based LES models (Sagaut 2002), may not hold (Ozgokmen, Iliescu & Fischer 2009). On the other hand, a possible shortcoming of the use of explicit spectral filtering as an SGS model (as done in this study) may lie in how accurately it replicates the energy transfer to the unresolved scales (Sengupta *et al.* 2009) and, thus, how well it estimates dissipation rates of kinetic energy and scalar variance.

Some answers to these questions are found in the analysis of Diamessis, Lin & Domaradzki (2008), who quantified explicit spectral filtering and penalty schemes in terms of the scale-dependent, effective numerical viscosity. Specifically, the numerical viscosity has a constant plateau followed by increasing values for scales close to the mesh cutoff. For a sufficiently fine mesh size, the plateau values are less than the molecular viscosity, indicating that the numerical dissipation does not affect the large scales of interest in this work. On the other hand, as expected, the scales of the order of the mesh size are strongly affected by the numerical dissipation. Therefore, given that the estimation of dissipation rates is not a focus of this paper, the associated shortcomings of explicit spectral filtering do not pose a major concern, and the use of more advanced SGS models (particularly the estimation model developed by the third author, Domaradzki, Loh & Yee 2002) will be left for future study. This choice is further motivated by the good agreement of the current numerical model with previous experimental, numerical and theoretical results for the mean wake flow and vorticity field structure (and the associated buoyancy-driven shear).

## 3. Initialization

### 3.1. *Replacing the sphere*

In a stationary horizontally periodic domain (§2.1), the introduction of a sphere would only allow for a spatially (and not temporally) evolving simulation. For the domain dimensions described in §4, a spatially evolving wake simulation could develop over a downstream distance no greater than $x/D = 10$ before the onset of spurious periodic interactions. For spatial development over larger downstream distances

$(x/D \approx O(10\,000))$, a complex coupling between a spherical grid near the sphere and a Cartesian one in the far wake would be necessary. Even if this coupling was efficiently implemented by replacing the Fourier discretization in the horizontal direction with a non-periodic, Legendre/Chebyshev polynomial-based, scheme (Cousin & Pasquetti 2004), the resolution of the far wake over a downstream distance $x/D \approx O(10\,000)$ would be prohibitively costly. As a result, any existing sphere-inclusive simulations of stratified wakes, using either low-order finite-differences (Hanazaki 1988) or spectral elements (Cousin & Pasquetti 2004), have been restricted to the near-wake and to body-based values of $Re$ in the range of [200, 300].

Constrained by the absence of the wake-generating sphere and driven by a focus on the intermediate-to-late wake physics, this study seeks an initial condition which will represent the near wake as accurately as possible and will allow a physics-based/transient-free transition into the NEQ regime. For all $Fr \geqslant 4$, the near wake is governed by three-dimensional turbulent dynamics over an $Fr$-dependent downstream distance of $x/D = (Fr/2)Nt \approx (Fr/2)\,2$ (Sp97), beyond which buoyancy forces begin to affect the larger scales of the flow. Near-wake dynamics are characterized by a wealth of complex phenomena such as boundary-layer separation (Chomaz *et al.* 1992), an attached core of absolutely unstable motion (Monkewitz 1988), a larger-scale helical mode (Chomaz *et al.* 1993*b*) and the presence of convectively unstable shear layers, radially positioned around the wake centreline. The destabilization by turbulence of these shear layers will quickly establish a self-similarly evolving wake structure (Bevilaqua & Lykoudis 1978). At some short distance downstream, the turbulence is in a state of equilibrium between turbulent dissipation and production (Dommermuth *et al.* 2002). Recent LES and DNS of stratified wakes (Gourlay *et al.* 2001; Dommermuth *et al.* 2002) have shown that in the above phenomena, the destabilization of the free shear layers is the most important for replicating the intermediate-to-late wake in both stratified and unstratified environments.

### 3.2. *Mean and fluctuating flow fields*

Following the above discussion, the initial flow field is chosen as the superposition of a mean velocity profile and a turbulent fluctuation field:

$$\boldsymbol{u}(x, y, z, t) = U_X(y, z, t) + \boldsymbol{u}'(x, y, z, t). \tag{3.1}$$

The subscript $X$ indicates averaging in the streamwise direction.

A variety of approaches may be found in the literature regarding the specification of the magnitude and distribution of the mean and fluctuating velocity fields in (3.1). Gourlay *et al.* (2001) chose the same axisymmetric Gaussian profile for both mean and fluctuating profiles but did not specify to what downstream location of a sphere wake these profiles corresponded. Dommermuth *et al.* (2002) used an axisymmetric Gaussian for the mean profile and the derivative of a Gaussian for the turbulence profile, both constructed by an approximation to the unstratified wake laboratory data of Bevilaqua & Lykoudis (1978) at $x/D = 6$. Brucker & Sarkar (2010) employed an approach similar to Dommermuth *et al.* (2002) but based their initial profiles at $Re = 10^4$ on the data of Bevilaqua & Lykoudis (1978) and at $Re = 5 \times 10^4$ on the data of Uberoi & Freymuth (1970). In addition, a criterion different from that of Dommermuth *et al.* (2002) was used to determine the termination point of the relaxation procedure. Finally, DDH employed the same Gaussian profile as Dommermuth *et al.* (2002) used for the mean velocity profile and extrapolated the structure of the fluctuating profile from measurements by Sp01 at $Nt = 9$ for $Fr = 4$.

This study employs the functional forms chosen by Dommermuth *et al.* (2002) for both mean and fluctuating flow fields, as these offer the most accurate representation of free shear layer-driven near-wake turbulence subject to balance between production and dissipation. The mean profile is given by

$$U_X(y, z) = U_0 \exp\left[ -\frac{1}{2}\left(\frac{y - y_0}{L_H}\right)^2 - \frac{1}{2}\left(\frac{z - z_0}{L_V}\right)^2 \right], \qquad (3.2)$$

where $y_0 = L_y/2$ and $z_0 = L_z/2$. Note that $U_0$ is the maximum centreline velocity and $L_H$ and $L_V$ are the initial horizontal and vertical length scales. Initially, $L_H = L_V$ and the streamwise-averaged spanwise and vertical velocities, $V_X = W_X = 0$. The initial $x$-averaged r.m.s. distribution of the fluctuating velocity is assumed to be axisymmetric and equipartitioned among its three components, an assumption valid for a wake that is actively turbulent over all its scales:

$$u'_X(r) = v'_X = w'_X = u_0 \left(1 + \frac{r^2}{r_0^2}\right) \exp\left(-0.5\frac{r^2}{r_0^2}\right) \qquad (3.3)$$

where $r = ((y - y_0)^2 + (z - z_0)^2)^{1/2}$, $r_0 = (y_0^2 + z_0^2)^{1/2}$ and $u_0$ is a characteristic turbulent fluctuation velocity. The actual values for $U_0$, $L_H$ and $u_0/U_0$ are prescribed as those corresponding to an axisymmetric wake assumed to be evolving self-similarly at $x/D = 2$ (see Appendix A for more details and the justification for the self-similarity assumption).

The three-dimensional fluctuating velocity field is constructed as spectrally random noise in three-dimensional Fourier space with a $k^{-5/3}$ energy spectrum. An inverse Fourier transform is applied to convert the noise into physical space and in the vertical the fields are projected on the non-uniform Gauss–Lobatto–Legendre grid of each subdomain. Finally, the data are windowed onto the envelope of the r.m.s. profile of (3.3). The use of white noise is avoided because it is unphysical and detrimental to the stability of the numerical solution.

Initially, the fluctuating and mean velocity fields are uncorrelated. In an under-resolved simulation, such as that considered here and the LES of Dommermuth *et al.* (2002), if the initial flow field is simply set as the superposition of the fluctuating and mean velocity fields, the turbulent fluctuations evolve independently of the mean and decay after only a few eddy turnover times, beyond which the mean flow decays strictly due to viscous effects. To avoid this behaviour, which is caused by the lack of correlation between fluctuating and mean velocity fields, a preliminary 'relaxation' simulation (Dommermuth *et al.* 2002) is run to generate a physically realistic velocity field. During relaxation, the flow is forced to maintain constant mean and r.m.s. fluctuating velocity profiles according to (3.2) and (3.3), while the spatial distribution of the turbulent fluctuations, and thus the Reynolds stresses, is allowed to vary. The relaxation is run for a time equal to approximately $10L_H/U_0$, i.e. roughly 10 local turnover times. At this point, production and dissipation reach an asymptotically steady state. Note that the well-resolved DNS of Gourlay *et al.* (2001) and Brucker & Sarkar (2010) did not require any relaxation procedure. A possible explanation for this difference is that both of these DNS studies, in contrast to those considered here and in Dommermuth *et al.* (2002), did resolve the fastest-growing modes of the radial shear layers, thus allowing the rapid formation of a well-correlated mean and fluctuating flow component before the unphysically premature decay of the latter.

Upon termination of the relaxation procedure, the downstream distance from the sphere is assumed to be equal to $x/D = 2$ (and not $x/D = 6$ as chosen by Dommermuth
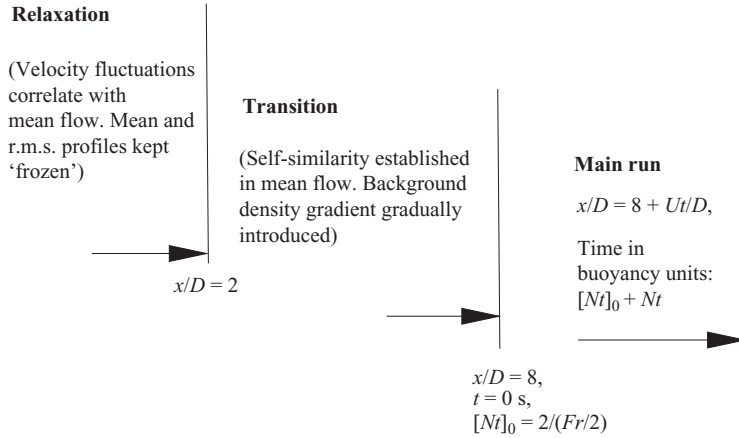
**Relaxation**

(Velocity fluctuations correlate with mean flow. Mean and r.m.s. profiles kept 'frozen')

**Transition**

(Self-similarity established in mean flow. Background density gradient gradually introduced)

$x/D = 2$

**Main run**

$x/D = 8 + Ut/D,$

Time in buoyancy units: $[Nt]_0 + Nt$

$x/D = 8,$
$t = 0$ s,
$[Nt]_0 = 2/(Fr/2)$

FIGURE 2. Stages in the simulation of a stratified turbulent wake: preliminary (relaxation and transition) and primary simulations. During the transition run, the buoyancy clock does not advance linearly with downstream distance $x/D$ to allow the gradual introduction of the ambient density gradient.

*et al.* 2002). As outlined in detail in Appendix A, the mean wake flow does not immediately behave self-similarly at this point. An additional preliminary simulation, a 'transition' run, is thus performed, where mean and fluctuating velocity profiles are allowed to adjust until self-similarity is established in the former. The transition run has a duration of $tU/D = 6$, which sets the equivalent of downstream distance from the sphere at the beginning of the primary simulation to be equal to $x/D = 8$. During the transition run, an initial fluctuating density field is generated by the evolving turbulent wake in an ambient density gradient (and the Brunt–Väisälä frequency $N$) that are gradually ramped to the desired value to avoid re-stratification-related transients, as elaborated in detail in Appendix B.

On account of the ramp-up of $N$ during the transition run, time in buoyancy units and downstream distance cannot be connected with the common expression $Nt = (x/D)/(Fr/2)$ (SBF96b). At the end of the transition run, buoyancy time is set to $Nt = [Nt]_0 = 2/(Fr/2)$ and physical time is set to $t = 0$ s. At this point, the primary simulation is started and, at any point therein, time in buoyancy units is given by $[Nt]_0 + Nt$. The equivalent downstream distance is given by $x/D = x_0/D + Ut/D$, where $x_0/D$ is equal to 8 and not 2 (see the previous paragraph). A schematic diagram of the different simulations (relaxation, transition and primary) and the relative positioning with respect to $x/D$, $Nt$ and time $t$ is given in figure 2.

Finally, when mean flow quantities are plotted in log-log coordinates as a function of $x/D$, growth/decay rates indicative of a self-similar behaviour of an unstratified wake are clearly visible at $x/D = 8$ (figure 7a–c). However, when plotting the same curves as a function of $Nt$ in log-log form, a change in slope is observed at small equivalent $x/D$ values, an artefact of the shift in origin when switching between $x/D$ and $Nt$ coordinates (figure 7b, c and f). Nonetheless, no change in slope is visible in these curves for $Nt$ equivalent to $x/D \geqslant 20$.

## 4. Numerical simulations

This paper considers results from six different numerical simulations of stratified turbulent wakes with non-zero net momentum at Reynolds number,

$Re = UD/\nu = 5 \times 10^3$ and $10^5$, and internal Froude number, $Fr = 2U/(DN) = 4, 16$ and 64. Hereafter, each run will be labelled as $RxFy$, where $x = Re/10^3$ and $y = Fr$. For all simulations, the values of $U$ and $D$ are the same. The Reynolds number and Froude number are varied by changing the values of $\nu$ and $N$, respectively. At a fixed $Re$ value, all $Fr$ simulations use the same relaxation run. The final result of this run is used to initialize the particular transition run for the desired $Fr$, where the mean density gradient is ramped-up to its designated value.

The computational domain has an initial horizontal dimension of $L_x \times L_y = 26\frac{2}{3}D \times 13\frac{1}{3}D$ and corresponds to a virtual stratified water tank of height $L_z = 12D$. Such a domain length is adequate to allow for multiple streamwise wavelengths of a vortex shedding instability. For values of $L_z$, $Re$, $Fr$ and initial wake height considered here, confinement of vertical wake growth due to turbulent entrainment (3D regime) or viscous diffusion (Q2D regime) is not an issue. Nevertheless, for $L_z = 12D$, simulations with $Fr > 200$ were not possible due to vertical confinement of viscously driven vertical growth of the Q2D wake.

The specific choice of initial domain width allows a lateral wake expansion until a value of $L_H = 0.15L_y$ before interactions with the wake's periodic image are established. To enable running late into the Q2D regime, the regridding technique of Gourlay *et al.* (2001) is periodically applied. Whenever $L_H = 0.08L_y$, the solution is re-interpolated onto a new domain with double the spanwise dimension and half the spatial resolution. Fourier interpolation is used to interpolate on the grid points within the original domain. On the new grid points outside the original domain, the solution is extrapolated as equal to the value at the previous domain boundary. These values are typically four or fewer orders of magnitude lower than their counterparts inside the wake core. Nonetheless, a pointwise discontinuity does develop at the location of the boundary of the original domain. Application of a Fourier spectral filter of order $p_F$ to the regridded solution in the spanwise direction eliminates this discontinuity. As a final check, the evolution of the vorticity field structure and the time series for $U_0$, $L_V$ and $L_H$ sampled from the onset of regridding until the time $L_H = 0.15L_y$ have been compared in regridded and non-regridded simulations. No significant differences are observed.

All simulations are forced to stop when the number of coherent structures remaining in the flow is inadequate to extract any meaningful mean flow statistics. This stopping point corresponds to a downstream distance $x/D \approx 5000$. The ability to run further in time (or for greater downstream distances) would require a longer domain that could accommodate at least double the number of pancake vortices in the late wake, i.e. a doubling in domain length, a change that the available computational resources cannot accommodate for the high-$Re$ runs.

The spectral multi-domain grids, with the horizontal direction employing a uniform grid, are shown in figure 3. Note that $M = 7$ and 13 non-uniform height subdomains of order of approximation $\hat{N} = 24$ and $\hat{N} = 40$ are used in the vertical direction at $Re = UD/\nu = 5 \times 10^3$ and $10^5$, respectively. The resolution at $Re = 5 \times 10^3$ and $10^5$ is $256 \times 128 \times 175$ and $512 \times 256 \times 531$ mesh points, respectively. Fourier and Legendre spectral filters of the order of $(p_F, p_L) = (20, 8)$ and $(10, 6)$ (see §2.4) are used in the low- and high-$Re$ runs, respectively. Figure 4 shows the filter functions used in this study.

Grid-independence was established at $Re = 5 \times 10^3$ by performing an $Fr = 4$ simulation with resolution $128 \times 64 \times 119$, corresponding to $M = 7$ subdomains of the order of $\hat{N} = 16$ in the vertical. The fine-grid resolution run produced nearly identical mean and fluctuating velocity profiles and streamwise spectra (over the
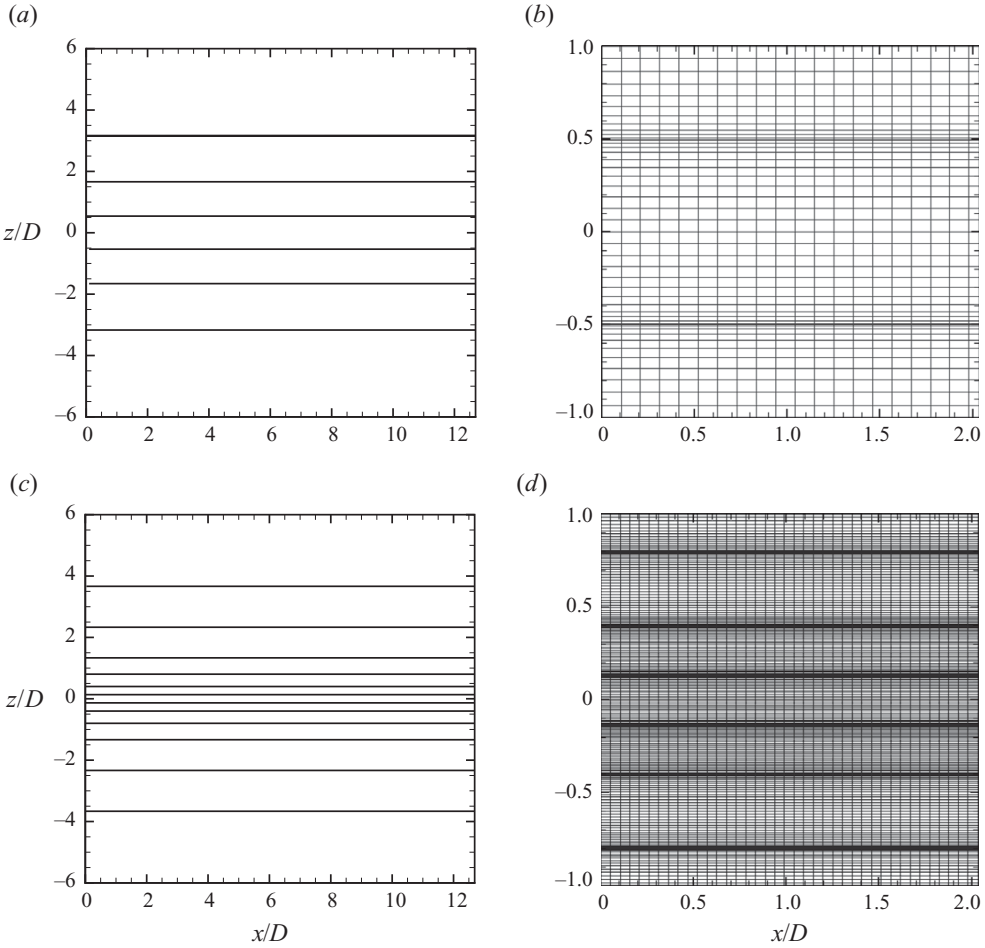
FIGURE 3. Streamwise truncated $Oxz$ section of the numerical grid employed in this study for the simulation of a stratified turbulent wake. In $(a, b)$ and $(c, d)$ the grid used for the simulations at $Re = 5 \times 10^3$ and $Re = 10^5$, respectively, is shown. In $(a, c)$ the full extent of the computational domain for each $Re$ is shown. The black solid lines delineate subdomain interfaces with the local Gauss–Lobatto–Legendre (GLL) grid omitted for clarity. In $(b, d)$ a zoomed view of the wake core region for each $Re$ with the local GLL grid included is shown. The $Re = 5 \times 10^3$ run employs $M = 7$ subdomains of the order of approximation $\hat{N} = 24$, with subdomain origins located at $z/D = -6, -3.17, -1.67, -0.5, 0.5, 1.67$ and $3.17$. The $Re = 10^5$ run employs $M = 13$ subdomains of the order of approximation $\hat{N} = 40$, with subdomain origins located at $z/D = -6, -3.67, -2.33, -1.33, -0.8, -0.4, -0.13, 0.13, 0.4, 0.8, 1.33, 2.33$ and $3.67$.

common range of resolved wavenumbers) over the entire wake evolution. The fine grid results are presented in this paper. In the higher-$Re$ runs, $\hat{N}$ ($p$-refinement) is increased and subdomain thickness ($h$-refinement) and spectral filter order are reduced to provide sufficient and numerically stable resolution of the volume-averaged vertical Taylor scale $l_z$, a typical measure of the thickness of the inclined vertical shear layers that develop in the intermediate-to-late wake (RdBK) (see figures 10 and 11). An *a priori* estimate of $l_z$ at $Re = 10^5$ may be obtained from the corresponding value observed at $Re = 5 \times 10^3$ by appealing to the scaling $l_z \approx Re^{-1/2}$ proposed by RdBK.
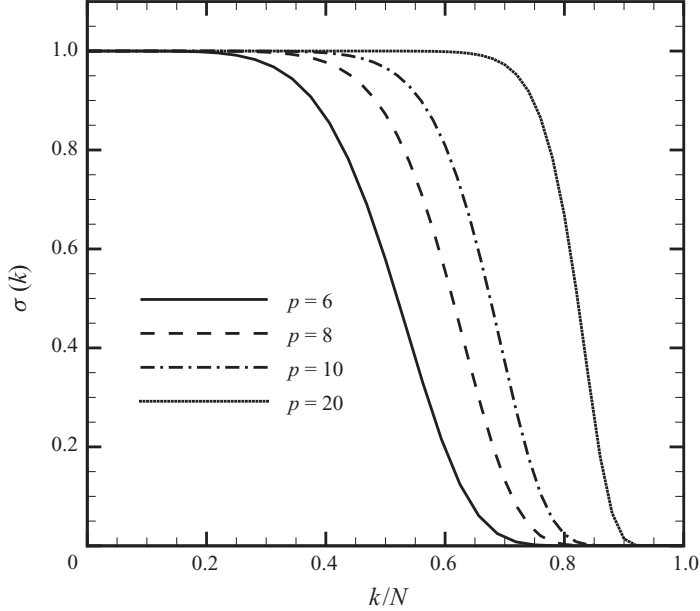
FIGURE 4. Exponential filter functions $\sigma(k/k_C)$ for the four different filter orders $p = 6$, 8, 10 and 20 used in this study. In Legendre space, $k$ and $k_C$ represent the mode number and total number of available modes, respectively. In Fourier space, $k$ and $k_C$ represent the two-dimensional wavenumber vector magnitude and the corresponding maximum value over all resolved horizontal wavenumbers, respectively.

According to Billant & Chomaz (2001), at high $Re$, $l_z \approx Fr^{1/3}$. Thus, if $l_z$ is adequately resolved at $Fr = 4$, it is also such at $Fr = 16$ and 64.

The adequacy of resolution for the $Re = 5 \times 10^3$ and $10^5$ simulations is evident in figure 5, which shows compensated one-dimensional (streamwise) spectra of the turbulent kinetic energy (averaged within the wake region) at $Nt = 1$, 30 and 70 for the $Fr = 4$ simulations. For the non-filtered range of scales, the form of all spectra in figure 5 is consistent with that observed in the mixed model LES of Dommermuth *et al.* (2002) (Gourlay *et al.* 2001 do not report any spectra for their stratified wake simulations). At $Nt = 1$, the R100F4 curve has significantly higher spectral content than its low-$Re$ counterpart, as shown by a fairly broad inertial range visible in the range $2.5 < k_x D < 15$. The effect of viscosity on the resolved scales of $Re = 5 \times 10^3$ is evident due to the more rapid drop-off of the spectrum within the range of scales directly unaffected by the filter. For all times shown and both $Re$, the energy spectra drop off smoothly at the higher range of wavenumbers not directly influenced by the filter and no sign of spectral blockage, i.e. spurious accumulation of energy at the highest resolved modes due to under-resolution, is observed (Boyd 2001). Instead, the filter produces artificial energy 'anti-accumulation' as shown by the sharp spectral slope in the range of wavenumbers it directly affects. Such behaviour should not be a cause for concern as the higher modes of the numerical solution are not necessarily physically correct (DDH). Finally, a very interesting difference between the two $Re$ is visible in the spectra at $Nt \geqslant 30$. The R5F4 curve has a very sharp slope for $k_x/D > 2.5$. In contrast, the R100F4 spectrum displays a much higher energy content at higher horizontal wavenumbers as shown by a pronounced $k_x^{-5/3}$ inertial range spanning almost a decade. This $-5/3$ signature is intimately linked to the flow structure
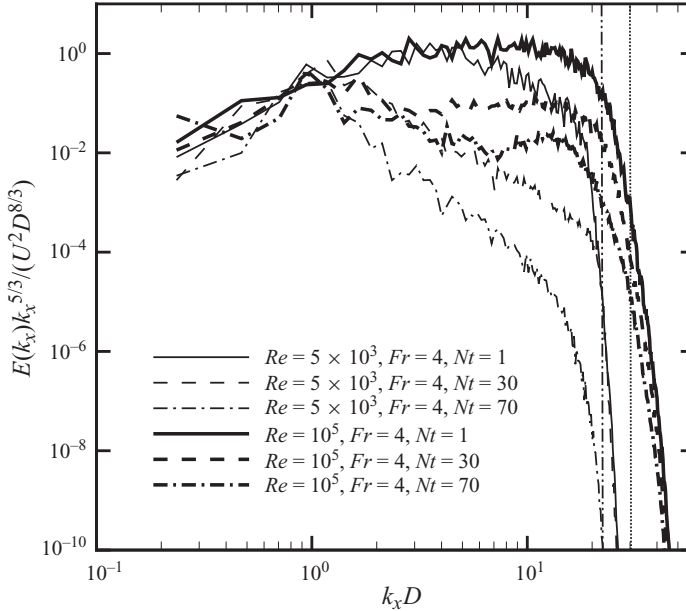
FIGURE 5. Compensated one-dimensional (streamwise) spectra of turbulent kinetic energy calculated for $Re = 5 \times 10^3$ and $10^5$. The spectra are averages of estimates taken at spanwise locations located in the interval $(y_0 - 2L_H, y_0 + 2L_H)$ on the horizontal centreplane. Spectra are sampled at different dynamical regimes of the wake evolution. Vertical lines represent the approximate limit over which the Fourier filter directly affects the numerical solution (dash-double dotted line, $Re = 5 \times 10^3$; dotted line, $Re = 10^5$).

observed in §5.2 and its implications are addressed briefly in §6.4. Finally, Legendre spectra in the vertical direction examined for all values of $Re$ and $Fr$ (not shown here) do not either show any signs of spectral blockage at the highest resolved modes.

Figure 3($d$) indicates that the $Re = 10^5$ runs employ 5 subdomains, i.e. 205 vertical grid points are assigned to the interval $-0.8 < z/D < 0.8$, i.e. a factor of 6 increase with respect to the simulations of Dommermuth *et al.* (2002), which assigned to the same portion of the wake core 35 uniformly spaced vertical grid points. In addition, the Legendre multi-domain technique has a very high order of accuracy and very weak artificial dissipation (explicitly controlled through high-order spectral filtering). Both these features have a distinct advantage over the second-order-accurate finite-difference scheme used by Dommermuth *et al.* (2002) in the vertical direction. The strong artificial dissipation of such a low-order scheme is further augmented by that driven by the inherently dissipative SGS model used by Dommermuth *et al.* (2002). On a similar note, the finite-volume-based DNS of Brucker & Sarkar (2010) initially assigned 100 grid points to the same spatial interval. However, as their simulations advanced in time, regridding was performed in both the horizontal and vertical directions, indicating that during the NEQ regime, not more than 50 grid points covered the central region of the wake.

The initial computational time step $\Delta t$ is chosen as such that the CFL stability criterion is obeyed in all three spatial directions for a third-order stiffly stable scheme. The following requirements are imposed:

$$\Delta t \frac{u_{max}}{\Delta x} < 0.18, \qquad \Delta t \frac{v_{max}}{\Delta y} < 0.18, \qquad 0.7 < \Delta t \left[ \frac{w}{\Delta z} \right]_{max} < 0.9. \qquad (4.1)$$

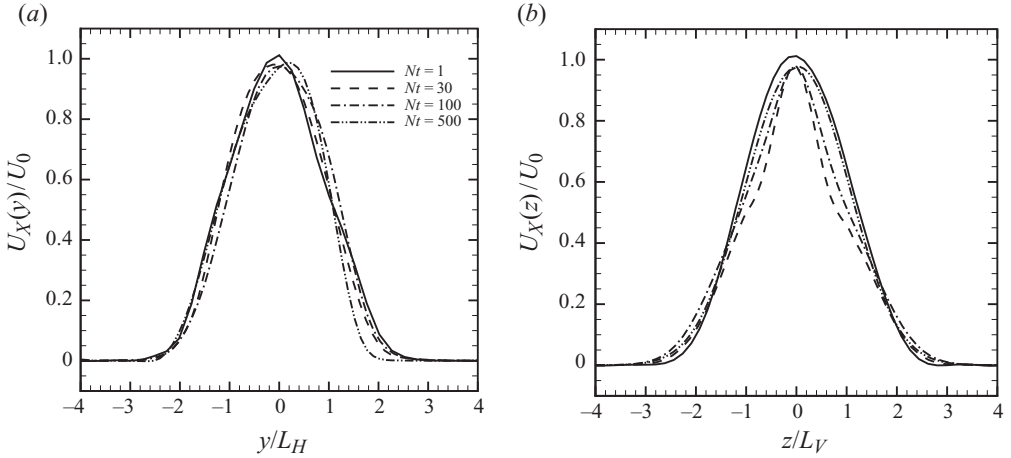(a)                                                    (b)



FIGURE 6. Self-similar scaling of $U_X(y, z)$ for four values of $Nt$ from 1 to 500 for $Re = 5 \times 10^3$ and $Fr = 4$. (a) $U_X(y)$ sampled on the $Oxy$ centreplane and (b) $U_X(z)$ sampled on the $Oxz$ centreplane.

In the $Re = 5 \times 10^3$ and $10^5$ runs, the time step at beginning of relaxation is set to $\Delta t/(D/U) = 0.0336$ and $0.0045$, respectively. The adaptive time-stepping scheme is activated whenever the time step reaches the lower or upper bound of the vertical CFL criterion and the time step is increased or decreased by a factor of 1.25, respectively. During relaxation, the time step weakly oscillates around its initial value. At the end of the primary simulations at low $Re$, the time step has increased by a factor of 10–40, the latter value corresponding to $Fr = 64$. The equivalent time step increase for the high-$Re$ simulations is a factor of 100–400. The maximum allowable time step is set at $\Delta t_{max} = 2\pi/(60N)$ to allow adequate resolution of one buoyancy period.

All simulations performed employ the MPI-based parallel implementation of the flow solver described in §2.3. The parallel solver scales linearly on up to 512 processors on a distributed memory cluster. The $Re = 5 \times 10^3$ runs use $\hat{N}_P = 32$ processors, whereas their $Re = 10^5$ counterparts require $\hat{N}_P = 256$. All simulations and post-processing were performed at the University of Southern California High Performance Computing Center's Linux cluster. On this machine, the average wall-clock time required for a computational time step is 5 and 14 s for the low- and high-$Re$ values, respectively. The respective durations of the 'relaxation' runs in wall-clock time were 15 h and 9 days. The primary simulations at $Re = 5 \times 10^3$ required between 16 and 24 h of wall-clock time. The wall-clock timings for the high-$Re$ simulations ranged between 14 and 36 days. For both $Re$, the $Fr = 64$ cases were the most costly.

## 5. Results

### 5.1. *Similarity scaling*

The similarity scaling of the characteristic mean velocity and length scales is first examined. The values of $U_0$, $L_H$ and $L_V$ are obtained from least-squares fitting a Gaussian, as defined by (3.2), to the $x$-averaged mean profile calculated at individual sampling times in the run evolution. As shown in figures 6(*a*) and 6(*b*) for run R5F4, and observed across all values of $Re$ and $Fr$, rescaling $U_X(y)$ and $U_X(z)$ with $U_0$, $L_H$ and $U_0$, $L_V$, respectively, leads to a satisfactory collapse of the profiles onto two single

curves, in agreement with the findings of SBF96b and Sp01. By virtue of the design of the initial condition (see §3), the mean velocity profile is self-similar at $x/D = 8$, corresponding to $Nt = 1$ for the curves of figures 6($a$) and 6($b$).

Figure 7($a$) shows the evolution of the mean centreline velocity $U_0$ as a function of $x/D$. At small values of $x/D$, i.e. in the 3D regime, all cases have a decay rate of $(x/D)^{-2/3}$ characteristic of unstratified axisymmetric wakes (Tennekes & Lumley 1972). This decay rate occurs over a window of $x/D$ values whose extent is proportional to $Fr$. The $-2/3$ power law is then followed by a much slower decay rate of $U_0$ which is responsible for higher values of $U_0$ with decreasing $Fr$ at a given $x/D$. As explained by Sp97, this reduced decay rate of the mean velocity may be attributed to re-stratification effects and the accompanying conversion of the available potential energy of the overturned isopycnals into horizontal kinetic energy, phenomena which intensify with decreasing $Fr$.

Following SBF96b and Sp97, $U_0$ is rescaled as $(U_0/U)Fr^{2/3}$ and is plotted as a function of $Nt$ (figure 7$d$). A satisfactory collapse of the $U_0(Nt)$ curves results across all $Fr$ for $Nt > 4$. During the 3D regime, use of $Nt$ units on the horizontal axis yields a decay rate which is lower than $(Nt)^{-2/3}$ (although figure 7$a$ clearly shows a $-2/3$ power law when plotting $U_0$ as a function of $x/D$). This result is an artefact of the shift in origin when switching between $x/D$ and $Nt$ coordinates (see the discussion in §3.2). Consequently, the exact beginning of the NEQ regime in $Nt$ units cannot be determined.

Nevertheless, for all simulations beyond $Nt = 4$, $U_0$ does have a reduced decay rate, the characteristic signature of the NEQ regime. Furthermore, the corresponding power-law exponent is very close to the $-1/4$ value observed by Sp97. For all $Re = 5 \times 10^3$ cases, the persistence of the reduced decay rate stops at some point within the interval $20 < Nt < 30$. Beyond this point, a faster decay rate is observed which compares well with the $(Nt)^{-0.76}$ power law reported by Sp97 for the Q2D regime. Sp97 not only identifies an NEQ-to-Q2D transition point of $Nt = 50$ for his wake experiments but also suggests that this value is flow-dependent. Thus, the earlier transition in the LES may result from the assumptions in designing the initial conditions.

An $(Nt)^{-0.76}$ power-law transition into the Q2D regime is also observed for the $Re = 10^5$ simulations. However, offsetting different $Fr$ curves in the vertical (figure 7$e$) shows a visible delay of this transition with respect to the low-$Re$ runs. The associated break-point occurs within the interval $60 < Nt < 120$, its location being $Fr$-specific. At a given $Fr$, the duration of the NEQ regime, as represented by the $-1/4$ power law in $U_0(Nt)$, is clearly prolonged with increasing $Re$. The oscillatory behaviour during $Nt \in [50, 200]$ for the R100F16 run is most likely not statistically significant and could be eliminated by performing more simulations at the given values of $Re$ and $Fr$, a strategy that could be pursued for all governing parameter values considered in this paper. Such a strategy would provide the additional benefit of a more precise determination of the end-point of the NEQ regime. Unfortunately, its computational cost is prohibitive, given the turnaround time of a single high-$Re$ run.

For all values of $Fr$ and $Re$, the wake-averaged half-width $L_H$ grows as $(x/D)^{1/3}$ (figure 7$b$), as observed in stratified wake experiments of Sp97 regardless of $Fr$ value and as is also representative of unstratified wakes (Tennekes & Lumley 1972). On account of the specific initial condition, the $1/3$ power law is established from the beginning of the simulations. Furthermore, it persists for the entire duration of the simulations, well into the Q2D regime, regardless of $Re$. Evidently, any $Re$-driven variation in flow structure does not appear to influence the wake's lateral growth rate.
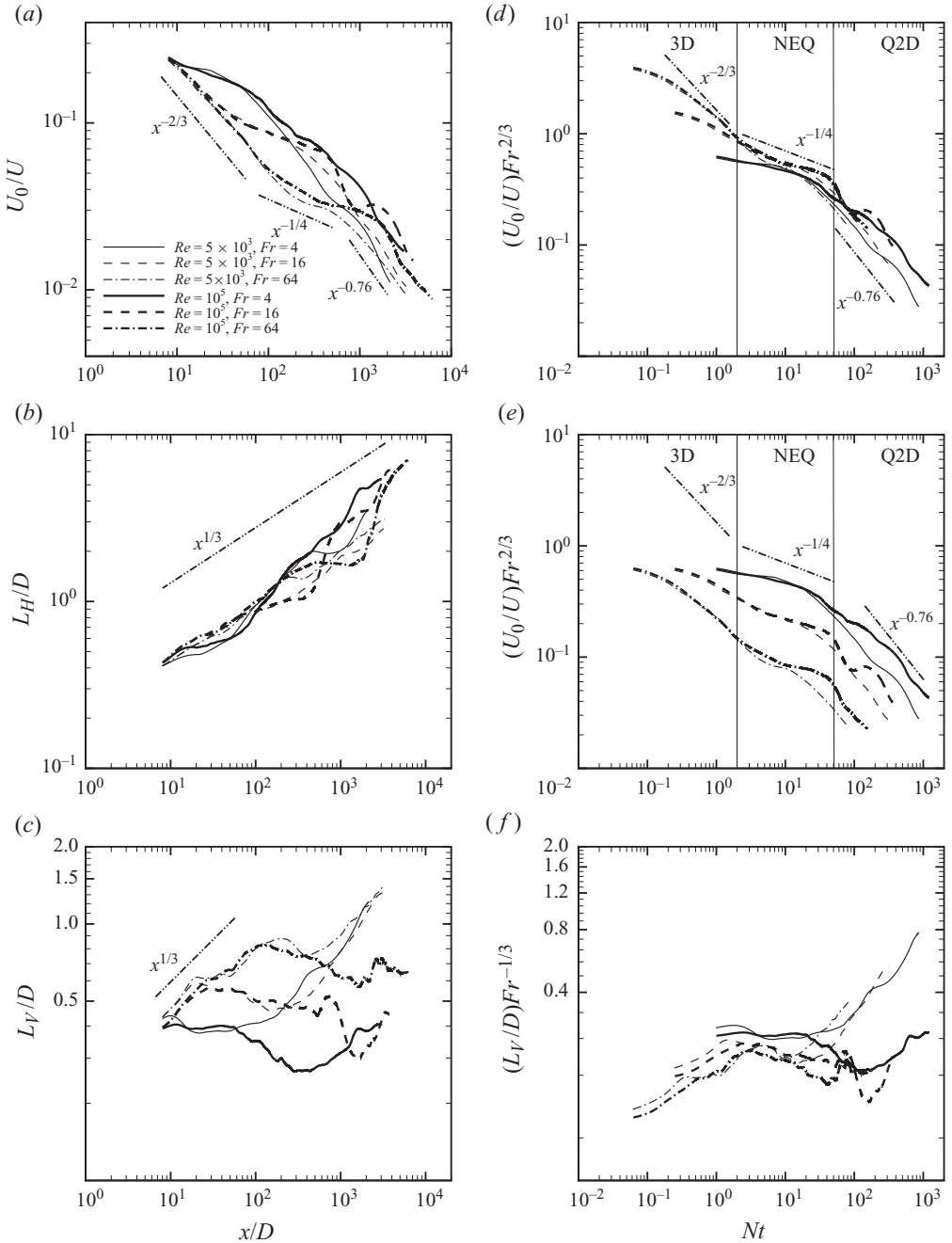
FIGURE 7. Evolution of mean centreline velocity, $U_0$, wake half-width, $L_H$, and half-height, $L_V$, for all simulations: (*a*) $U_0(x/D)$, (*b*) $L_H(x/D)$, (*c*) $L_V(x/D)$, (*d*) $U_0(Nt)$, (*e*) $U_0(Nt)$ with $Fr = 16$ and 64 rescaled by factors of 0.4 and 0.16, respectively, and (*f*) $L_V(Nt)$. Dashed lines represent power laws observed in the laboratory experiments of Spedding or proposed by Meunier *et al.* (2006). Line legend is given in (*a*). The thin vertical lines delineate transition points between regimes as identified in the low-*Re* experiments of Spedding (1997).

Similar to $L_H$, for all runs, the wake-averaged half-height $L_V$ has a 1/3 growth rate up to an ($x/D$) value corresponding to $Nt \approx 2$. Beyond this point, $L_V$ remains constant (figure 7c) as the NEQ regime is established. In the low-$Re$ runs, $L_V$ begins to grow again at large values of $x/D$, which is apparently set by $Fr$. The scaling arguments of Meunier *et al.* (2006) suggest that such a growth is viscously driven and characterized by a 1/2 growth rate. A least-squares power-law fit to the late-time growth phase of $L_V$ yields an exponent in the range of $[0.36, 0.48]$ across the different $Fr$ values. However, these exponents are inferred from an interval with relatively short duration in $Nt$ units. For the current problem configuration, runs to higher values of $Nt$ are not possible due to vertical confinement effects. Furthermore, the diffuse inclined spanwise vorticity layers dominating the late-time low-$Re$ wake (figure 11) exhibit a strong streamwise correlation which would require extremely long domains to accommodate a sufficient number of such flow structures and extract any meaningful statistics. Now, in all high-$Re$ runs, $L_V$ has a constant value starting at $Nt \approx 2$ and extending to the end of the simulation. Late-time oscillations are directly linked to the small number of coherent structures in the streamwise direction (figure 11).

In terms of $Fr$ scaling of the near-constant value of $L_V$ in the NEQ regime, a natural choice would be that $L_V$ scales as $Fr^{1/3}$ (figure 7f), as also proposed by Meunier *et al.* (2006). However, the empirical value of $Fr^{1/4}$, significantly removed from the $Fr^{0.6}$ scaling proposed by Sp02, was found to collapse the data even better. This lack of agreement between LES and self-similarity model and experiments indicates that any numerically computed early-time value of $L_V$ cannot be truly claimed to be an independent outcome of the LES instead of an actual input.

Although it has not been possible to determine the exact temporal location of the break-point for the transition from NEQ to Q2D dynamics, the persistence of constant $L_V$ and the prolonged interval of reduced decay rates of $U_0$ at high-$Re$ clearly indicate a Reynolds number dependence in wake dynamics. Dommermuth *et al.* (2002) (their figures 5 and 6) also report similar behaviour for $U_0$ and $L_V$ but do not investigate it in detail. An examination of the development of the vorticity field structure across the full range of $Re$ and $Fr$ values can provide critical insight towards understanding the mechanism underlying this $Re$-dependence. Similar observations have been made by Brucker & Sarkar (2010) who associated the particular behaviour of $U_0$ and $L_V$ in the NEQ regime with a decay rate of the turbulent kinetic energy dissipation rate with inertial, and not viscous, scaling but deferred further discussion to future work.

### 5.2. *Vorticity field*

Contour plots of the vertical vorticity $\omega_z$ on the $Oxy$ centreplane of the flow (sampled at times $Nt = 1, 10, 30, 70, 160, 400$ and $1100$) are shown in figures 8 and 9. The R5F4 results are qualitatively similar to those observed in the laboratory (Sp97) and DNS/LES (Gourlay *et al.* 2001; Dommermuth *et al.* 2002) at comparable $Re$ and $Fr$. The early-time vorticity field has a structure characteristic of a non-stratified wake. By $Nt \approx 30$, the $\omega_z$ field transitions into a more organized structure with pancake vortices beginning to emerge. Subsequently, the wake grows in the spanwise direction through pairing interactions among like-signed vortices and through diffusion. A vortex pairing event is discernible in the left end of the domain, at $Nt = 160$. The low-$Re$ $\omega_z$ fields for $Fr = 16$ and 64 (not shown here for the sake of economy) have a similar structure. In agreement with Sp97, at a given $Nt$ value, higher $Fr$ is associated
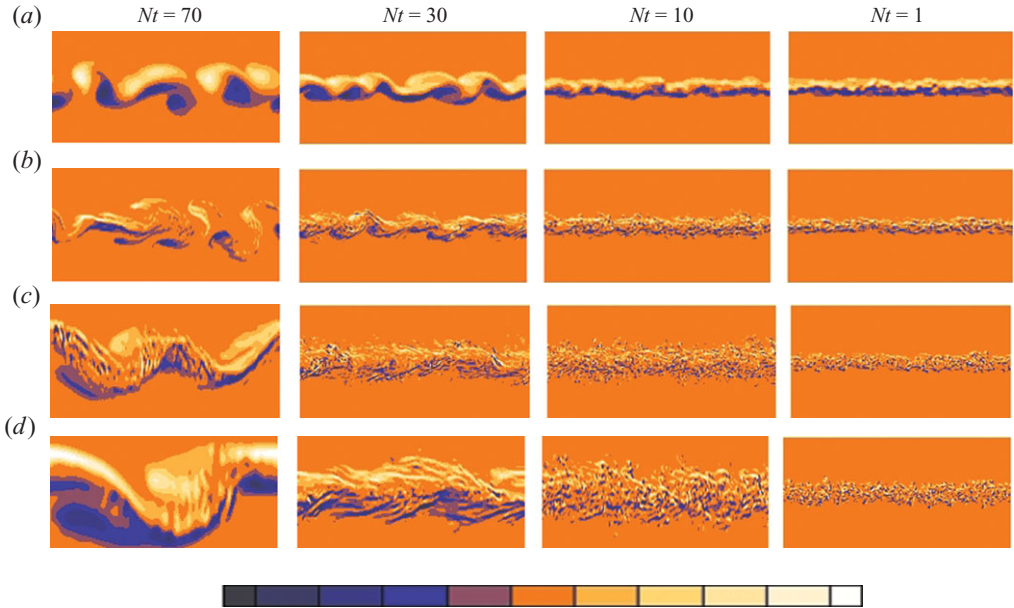
FIGURE 8. Contour plots of $\omega_z$ sampled at different times on a $26\frac{2}{3}D \times 13\frac{1}{3}D$ subsection of the $Oxy$ centreplane for simulations: (*a*) R5F4, (*b*) R100F4, (*c*) R100F16 and (*d*) R100F64. The sphere travels from left to right. At each snapshot, the colour bar is rescaled locally, and symmetrically, about $\omega_z = 0$ to $\pm(|\omega_z^{max}| + |\omega_z^{min}|)/2$. The minimum/maximum range for the colour bar for $\omega_z/(U/D)$ at $Nt = 70$ for each simulation is (*a*) $[-0.12, 0.12]$, (*b*) $[-0.31, 0.31]$, (*c*) $[-0.18, 0.18]$ and (*d*) $[-0.012, 0.012]$.

with late-time coherent vortices of larger horizontal length scale (when normalized with the sphere diameter $D$).

At $Re = 10^5$, the very early-time ($Nt = 1$) $\omega_z$ field has significantly more fine-scale structure as compared with its low-$Re$ counterpart. If one now focuses on the R100F4 case, a larger-scale vortical structure, a precursor to pancake formation, is visible in the contours of $\omega_z$ by $Nt = 30$. However, persistent finer-scale motions are visible within this footprint of the pancake vortices. The smooth drop-off of the spectra in figure 5 strongly indicates that these finer-scale motions are physically driven and not numerical noise driven by under-resolution.

With increasing $Fr$ (i.e. in runs R100F16 and R100F64), the $\omega_z$ field at a given $Nt$ occupies a broader spanwise extent, in agreement with figure 7(*b*). A very rich fine-scale structure is also present at $Nt = 30$ for both $Fr = 16$ and $64$ at $Re = 10^5$. Starting at $Nt = 70$ and $50$ for $Fr = 16$ and $64$, respectively, striations inclined obliquely to the wave axis are visible. The peaks in these striations are separated by 8–16 grid points and the corresponding streamwise spectra are similar to those in figure 5, i.e. show no tendency for spuriously generated blockage (Boyd 2001), proving that such flow structure is indeed physical.

Figures 10 and 11 show the spanwise vorticity $\omega_y$, sampled over a sub-window on the $Oxz$ centreplane of the flow at times $Nt = 1, 30, 50, 70, 100$ and $200$. The size of the visualization window is chosen as such to best illustrate characteristic features of the spanwise vorticity field, i.e. the inclined shear layers and, at high $Re$, any resulting coherent vortex structures. At $Nt = 1$, the R5F4 case has a $\omega_y$ field typical of active three-dimensional turbulence which gradually, through the effect of buoyancy, transitions into a structure characterized by distinct inclined layers,
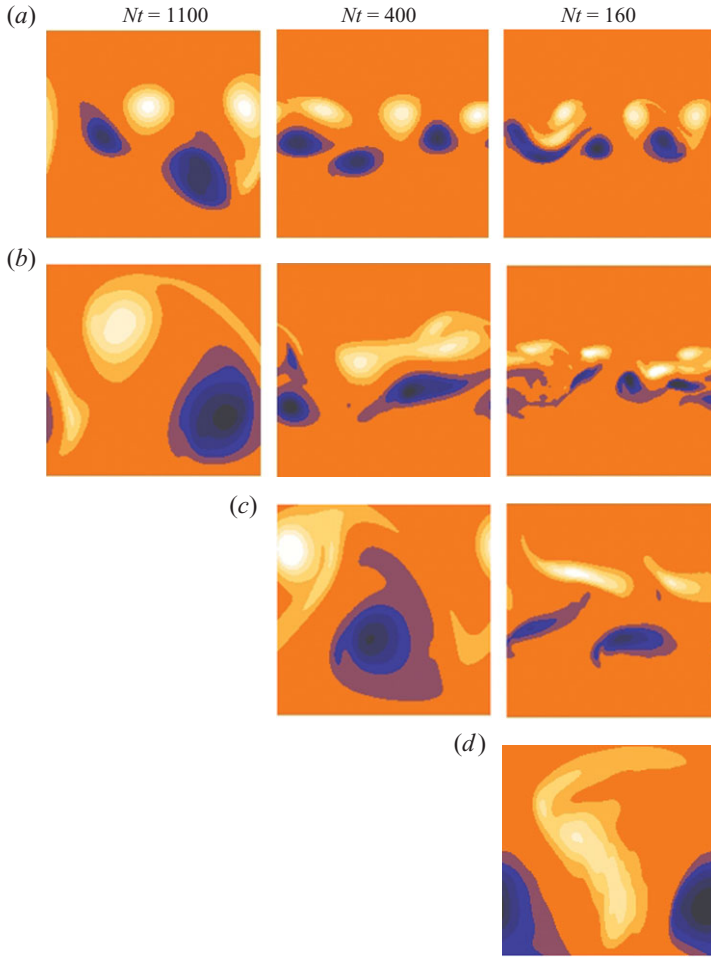
FIGURE 9. The same as in figure 8, but with snapshots sampled at later times of wake evolution and with $Oxy$ centreplane subsection dimensions of $26D \times 26\frac{2}{3}D$.

symmetrically positioned with respect to the wake centreline. Weak undulations are visible along these layers at $Nt = 30$ but they quickly disappear as the layers become more diffuse and stable to any shear instability. The inclination of these diffuse shear layers increases with time due to the enhanced advection of vortex lines by the mean flow at the wake centreline with respect to the periphery (Sp02). The structure of the low-$Re$ $\omega_y$ fields for $Fr = 16$ and 64 (not shown here) evolves in a similar manner, as previously reported by Sp02. At $Nt \approx 40$, the $\omega_y$ field is dominated by inclined diffuse layers. In agreement with the low-$Re$ scaling originally proposed by Godoy-Diana, Chomaz & Billant (2004), the layer thickness does not demonstrate an $Fr$-dependence and appears to be controlled strictly by viscosity.

The early-time $\omega_y$ fields for all high-$Re$ simulations have an actively turbulent structure which also transitions into an arrangement of inclined shear layers by $Nt = 30$. However, these shear layers are much thinner than their low-$Re$ counterparts and have a much higher magnitude of $\omega_y$. Moreover, at a given value of $Fr$ and $Nt$, the high-$Re$ wake has a larger number of layers inside the wake core.
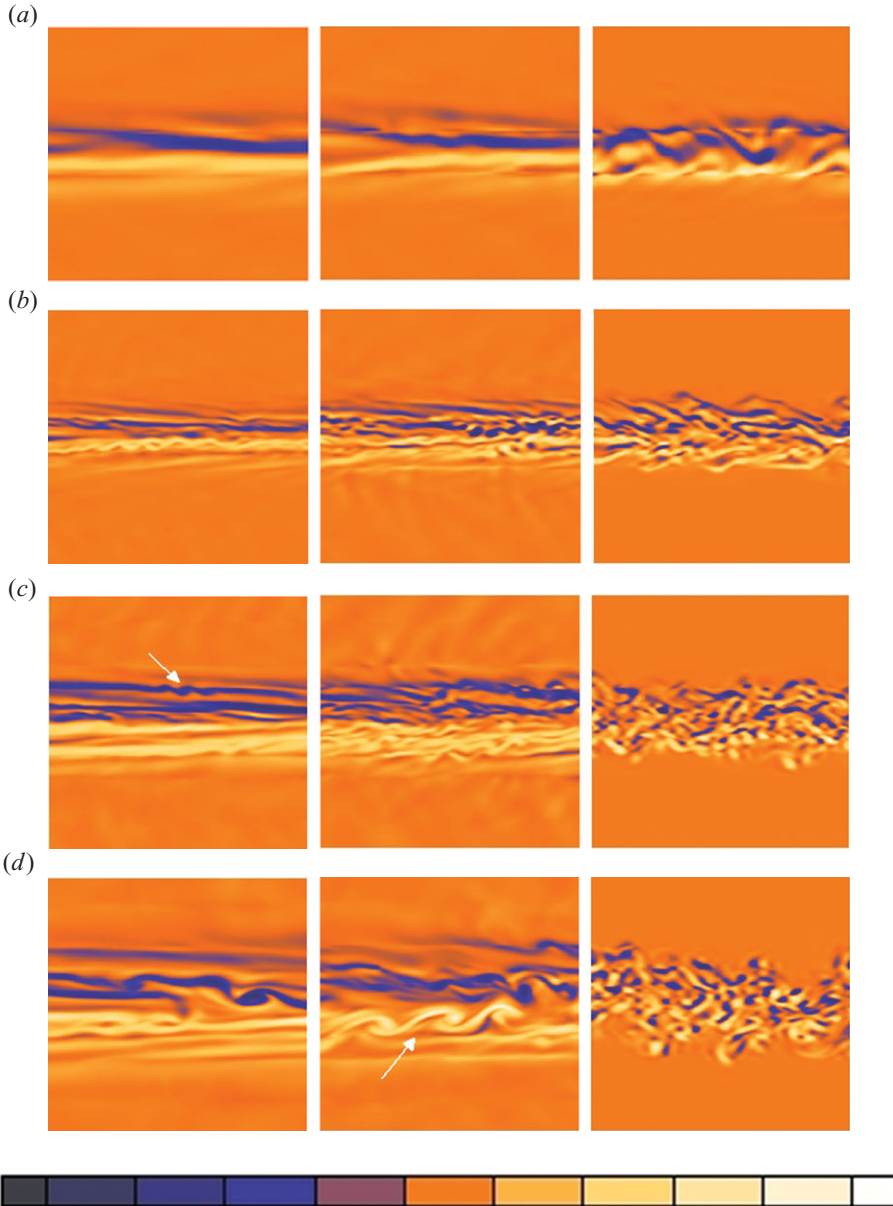
(*a*)

(*b*)

(*c*)

(*d*)



FIGURE 10. Contour plots of $\omega_y$ on a $6D \times 6D$ subsection of the $Oxz$ centreplane for simulations: (*a*) R5F4, (*b*) R100F4, (*c*) R100F16 and (*d*) R100F64. Times shown (from right to left) are $Nt = 1$, 30 and 50. As in figure 8, the sphere travels from left to right. White arrows point to distinct Kelvin–Helmholtz instabilities. At each snapshot, the colour bar is rescaled locally, and symmetrically, about $\omega_y = 0$ to $\pm(|\omega_y^{max}| + |\omega_y^{min}|)/2$. The minimum/maximum range for the colour bar for $\omega_y/(U/D)$ at $Nt = 50$ for each simulation is (*a*) $[-0.36, 0.36]$, (*b*) $[-1.25, 1.25]$, (*c*) $[-0.32, 0.32]$ and (*d*) $[-0.1, 0.1]$.

Focusing now on the R100F4 case, significant finescale disturbances are embedded within the shear layers, possibly a residual of the highly energetic initial turbulence. These disturbances are often organized in near-circular coherent patches. An even more visibly organized vorticity structure has emerged at $Nt = 70$ in the form of
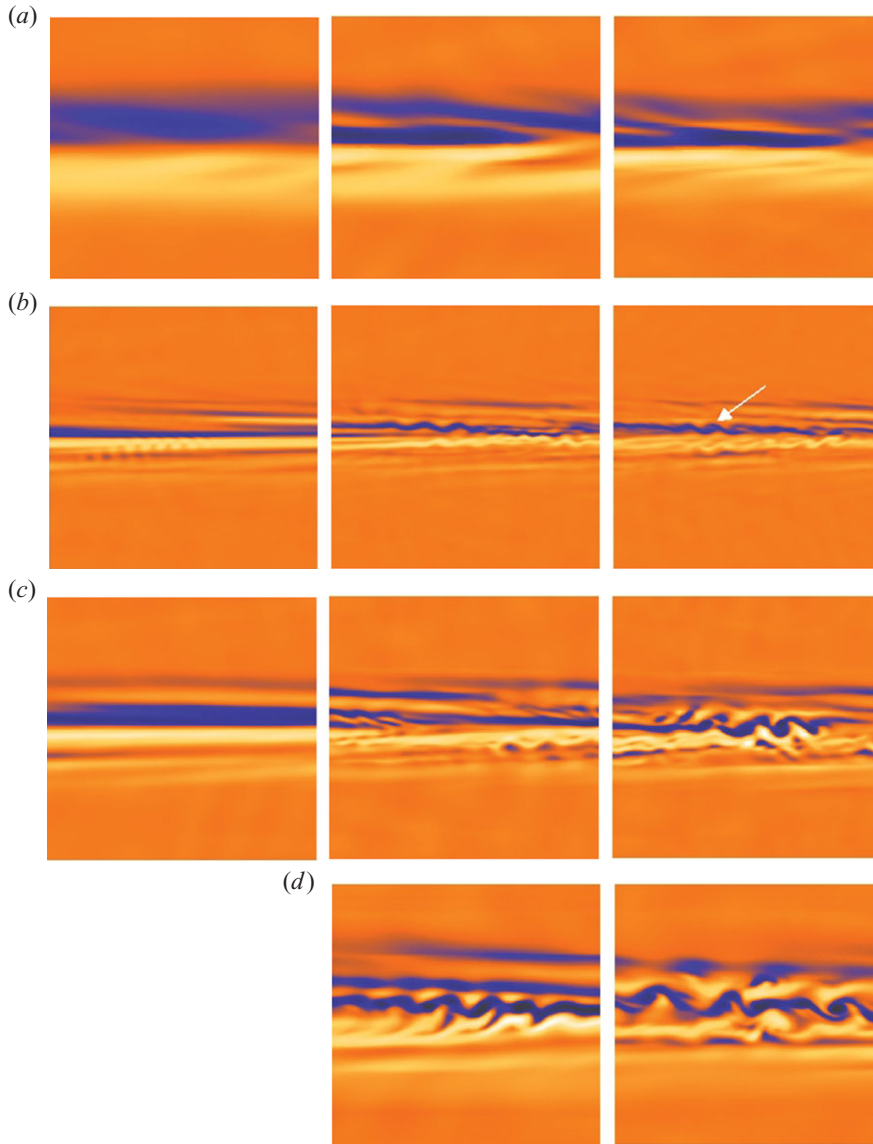
FIGURE 11. The same as in figure 10, but with snapshots sampled at $Nt = 70$, 100 and 200.

secondary Kelvin–Helmholtz instabilities. Such secondary instabilities are found to occur until $Nt \approx 100$. Weak undulations still develop along the layers at as late as $Nt \approx 200$, beyond which the layers evolve into a stable configuration with their thickness growing due to viscous diffusion.

A similar qualitative picture is observed for the R100F16 and R100F64 cases, although identifiable quantitative differences do exist across Froude numbers. At all $Nt$ values examined, the strength of the shear layers diminishes with increasing $Fr$, whereas their thickness appears to increase. Secondary Kelvin–Helmholtz instabilities are also observed until $Nt \approx 100$ but, by $Nt = 200$, the remaining inclined shear layers are more stable than their $Fr = 4$ counterparts at high $Re$.
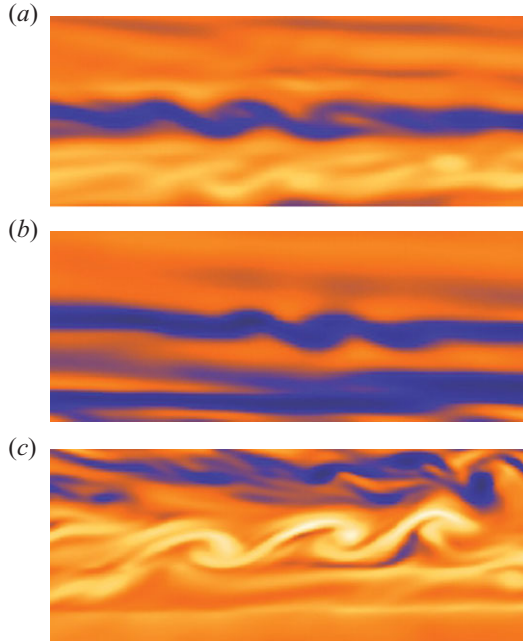
FIGURE 12. Contour plots of $\omega_y$ at select times showing Kelvin–Helmholtz instabilities (indicated by white arrows in figures 10 and 11) on a $3D \times 1.2D$ subsection of the $Oxz$ centreplane for simulations: (*a*) R100F4 ($Nt = 70$), (*b*) R100F16 ($Nt = 50$) and (*c*) R100F64 ($Nt = 30$). Colour bar and sphere motion are the same as in the corresponding panels of figures 10 and 11.

It is noteworthy though that the emergence of distinct secondary Kelvin–Helmholtz instabilities, in the form of visible billows standing out against any residual turbulent fine structure, occurs at earlier times with increasing *Fr*. Figure 12 shows zoomed views of the instability events indicated by a white arrow in figures 10 and 11. These Kelvin–Helmholtz billow trains are concentrated near the planes of maximum vertical shear (see figure 14) with each train consisting of three to five billows.

Contour plots of $w$ sampled over one of the planes of maximum vertical shear (see figure 14) at times $Nt = 30$ and 70 for case R100F4 (figure 13; cases R100F16 and R100F64 exhibit similar behaviour) show that the secondary instabilities are organized in localized concentrations of high $w$-velocity of bands of alternating signs, a characteristic signature of Kelvin–Helmholtz billow trains. Normalization with the corresponding mean centreline velocity at the specific times identifies events where $w/U_0 \approx \pm 0.2$ and $w/U_0 \approx \pm 0.1$ at $Nt = 30$ and $Nt = 70$, respectively. These events are clearly capable of driving significant local vertical transport. Two-dimensional vertical transects normal to the axis of the $w$-velocity contour bands are found to show the horizontal vorticity structure typical of Kelvin–Helmholtz instabilities shown in figure 12. When observed over time, these striations are not found to propagate into the far field of the wake and their $w$-velocity magnitude is much larger than that of wake-radiated internal waves (Bonneton *et al.* 1993). Both these observations indicated that the striations under consideration should not be misconstrued as internal waves.

For the high-*Re* values considered here, 20–40 vertical grid points are found to span the thickness of the shear layers visible at $Nt \approx 30$ for $Fr = 4$ and 64, respectively. In addition, 40–60 vertical grid points span individual Kelvin–Helmholtz billows at
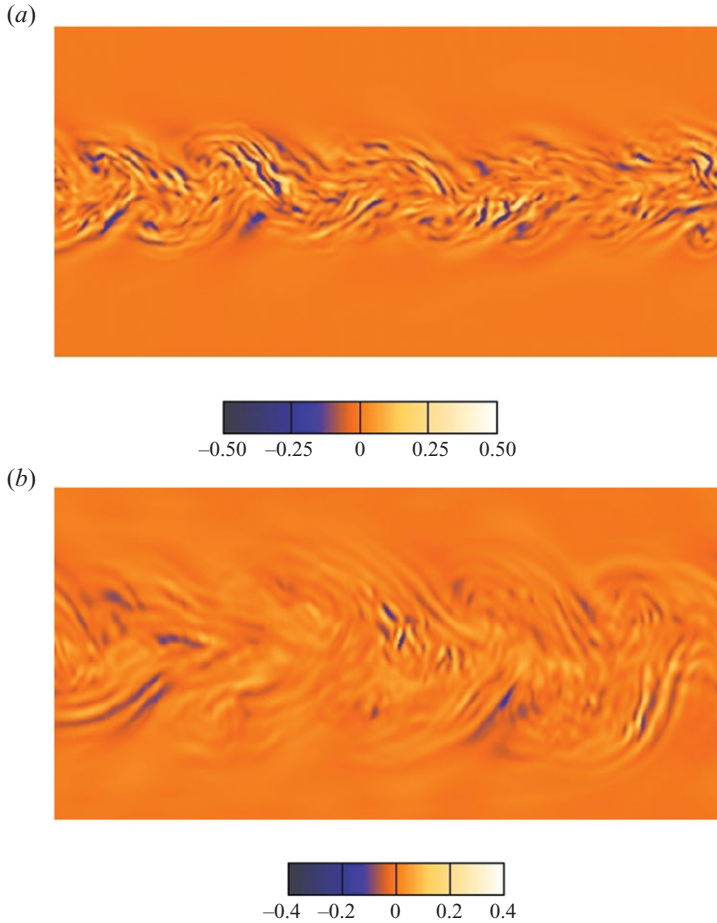
(*a*)



(*b*)



FIGURE 13. Contour plots of vertical velocity for simulation R100F4 at times $Nt = 30$ (*a*) and 70 (*b*) normalized by the respective value of the mean centreline velocity $U_0$. Contours are shown on a $26\frac{2}{3}D \times 13\frac{1}{3}D$ subsection of the $Oxy$ plane centred on the wake centreline and sampled at the location of the lower peak of the corresponding mean-squared vertical shear profile in figure 14. The patches of striations of alternating sign, slightly offset from the wake centreline and inclined obliquely to it, correspond to billows of secondary Kelvin–Helmholtz instabilities, as also observed in figure 9 of Riley & de Bruyn Kops (2003) and figure 4 of Hebert & de Bruyn Kops (2006).

all Fr values. The horizontal dimension of these billows is resolved with 10 to 16 streamwise grid points. These observations of flow feature resolution and the structure of the spectral filter functions in figure 4 indicate that the primary two-dimensional stage of the Kelvin–Helmholtz instability and the pairing between successive billows are well-resolved.

For the resolutions reported above, features of the subsequent nonlinear evolution of the observed secondary Kelvin–Helmholtz instabilities, i.e. the formation of braids between successive billows and the transverse instabilities and transition to turbulence within an individual billow, are either marginally resolved or totally unresolved and, thus, controlled by the spectral filter. It is the spectral filter that ultimately drives the dissipation of the energy within these secondary motions. Since this dissipation is effectively balanced out by the flux of energy to unresolved scales, driven by the

Kelvin–Helmholtz billows, which are well-resolved with a highly accurate spectral discretization, the numerically replicated evolution of the secondary instabilities is deemed accurate for the scope of this study, i.e. demonstrating that formation of secondary Kelvin–Helmholtz instabilities is indeed possible within the core of a stratified turbulent wake at sufficiently high $Re$. Given the high-$Re$ run times reported in §4, a sensitivity study of the effect of the spectral filter order and possibly enhanced resolution on the full nonlinear evolution of the localized Kelvin–Helmholtz instabilities is not within available computational resources.

### 5.3. *'Stratified turbulence' and buoyancy-driven shear in high-Re wakes*

The larger-scale quasi-horizontal motions and secondary instabilities and turbulence embedded therein, observed in the high-$Re$ stratified wakes of §5.2, are similar to the flow structure reported in the numerical investigation of RdBK, Waite & Bartello (2003), Laval *et al.* (2003), Winters *et al.* (2004), Brethouwer *et al.* (2007) and Deloncle *et al.* (2008). The mechanism responsible for these secondary events appears to be the gradual decorrelation of horizontal layers in a high-$Re$ stratified environment which leads to localized regions of intensified vertical shear, as proposed by Lilly (1983). One favourable pathway towards this flow state, which is highly prone to shear instability, is the zigzag instability of a pair of counter-rotating columnar vortices (Billant & Chomaz 2000*a,b*). Furthermore, Majda & Grote (1997) showed that a pre-existing vertical shear will be intensified in a stable density gradient and, thus, the Kelvin–Helmholtz waves and instabilities seen here could develop faster through such a mechanism. In contrast to the previous numerical studies of RdBK, Winters *et al.* (2004), Brethouwer *et al.* (2007) and Deloncle *et al.* (2008), however, we note that the tendency towards layer decorrelation and intensification of vertical shear in a stratified wake is not pre-set as part of the initial conditions, but emerges from the initial turbulent conditions, much as it does in the laboratory and presumably, in nature. To this end, the initial conditions of Waite & Bartello (2003) and Laval *et al.* (2003) are indeed turbulent but, on account of their statistically homogeneous nature, do not correspond to a canonical localized turbulent flow.

The vertical distribution and magnitude of buoyancy-driven vertical shear in a stratified wake and its dependence on $Re$ and $Fr$ are best quantified through the analysis followed by RdBK. Specifically, the horizontally averaged mean-squared vertical shear, $S^2(z)$ is defined as

$$S^2(z) = \left\langle \left( \frac{\partial u}{\partial z} + \frac{\partial v}{\partial z} \right)^2 \right\rangle_H, \qquad (5.1)$$

where $\langle \cdot \rangle_H$ represents averaging over the interval $[0, L_x]$ and across a transverse interval $[-2L_H, 2L_H]$ on the $Oxy$ centreplane. The evolution of $S^2(z)$ is shown in figure 14 for case R100F4, and $S^2(z)$ peaks always at $z/D \approx \pm 0.2$, which nearly coincides with the location of maximum vertical shear of the mean velocity profile $U_X(y, z)$. It is at these locations where the most vigorous secondary Kelvin–Helmholtz instabilities occur (such as those shown in figure 12). The peak value of $S^2(z)$ diminishes rapidly at early times but, starting at $Nt = 30$, decays at a slower rate, with its vertical extent being progressively restricted to the $Oxy$ centreplane. This observation is consistent with the increased localization of any secondary instabilities to the immediate vicinity of this centreplane as time advances. At the higher-$Fr$ values for $Re = 10^5$, $S^2(z)$ (not shown here) evolves in a manner similar to figure 14, the main difference being a reduction of the peak values with increasing $Fr$ at given $Nt$. Finally, for a given $Fr$ value, the $S^2(z)$ profile (not shown here) for the lower-$Re$ simulation has a peak
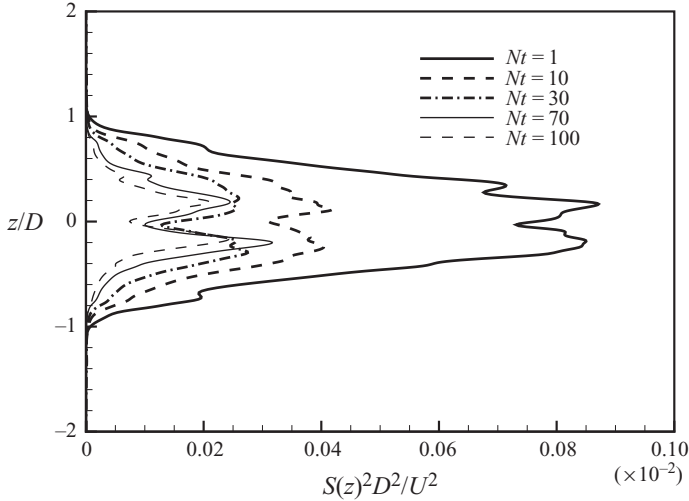
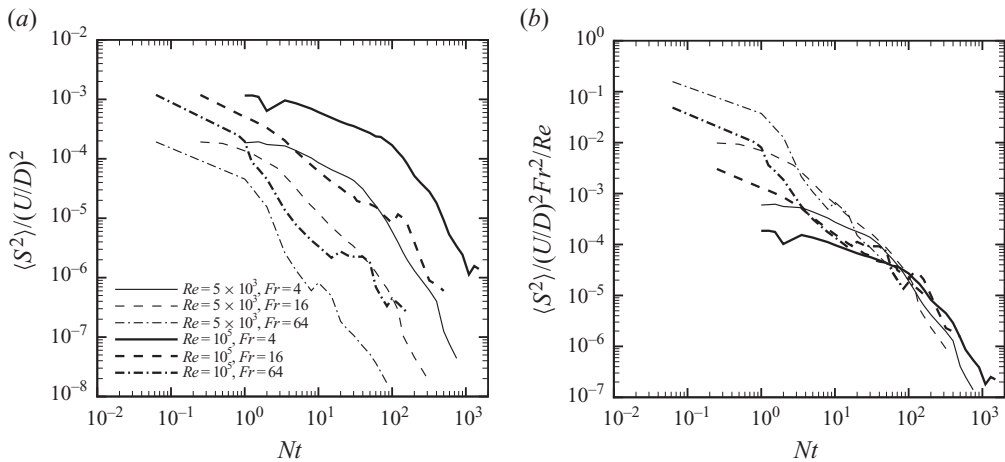FIGURE 14. Profile of the mean square vertical shear for case R100F4 as a function of time.



FIGURE 15. (*a*) Evolution of the mean square vertical shear integrated over the volume of the wake. (*b*) Same quantity but rescaled with $Fr^2/Re$ according to scaling proposed by Riley & de Bruyn Kops (2003) and Spedding (2002).

that occurs at a comparable location, with somewhat greater offset from the wake centreline, but diffuses out much faster than its high-*Re* counterpart.

The *Re*- and *Fr*-dependence of the magnitude of buoyancy-driven shear is best illustrated by further averaging $S^2(z)$ in the vertical direction over a window $[-2L_V, 2L_V]$ (figure 15*a*). At a given *Fr*, from the onset of the simulations up to $Nt \approx 10$, the higher *Re* exhibits an average shear magnitude squared that is a factor of 15–20 greater than the corresponding low-*Re* value. At a given *Re*, for $Nt > 10$, increasing *Fr* corresponds to weaker shear magnitude.

A scaling may now be sought to collapse the time series in figure 15(*a*). Stratification may be accounted for through the $Fr^{-2}$ scaling proposed by Sp02. The effect of Reynolds number may be addressed by following RdBK. The contribution of the

vertical shear to the dissipation term in the kinetic energy equation may be written as

$$\frac{1}{Re}\left\langle \left(\frac{\partial u}{\partial z} + \frac{\partial v}{\partial z}\right)^2 \right\rangle = \frac{1}{Re}S^2, \tag{5.2}$$

where the operator $\langle \cdot \rangle$ indicates averaging over the volume of the wake (as defined by the window $[-2L_H, 2L_H] \times [-2L_V, 2L_V]$ centred on the wake centreline). The fully resolved DNS of RdBK obtained an accurate estimate of the kinetic energy dissipation rate which, upon the establishment of stratified turbulence, was found to be independent of $Re$. RdBK further suggested that $S^2/Re$ is also approximately independent of $Re$. Assuming that this $Re$-independence also holds in the wake simulations considered here, the volume-averaged mean-squared vertical shear (the term in the brackets on the left-hand side of (5.2)) scales with $Re$. Such a scaling was also proposed by Praud, Fincham & Sommeria (2005) for stratified turbulence at sufficiently high Reynolds numbers. Thus, the appropriate scaling that combines the effect of both stratification and Reynolds number is $Re/Fr^2$. As is evident in figure 15(*b*), this scaling provides a satisfactory collapse of the $S^2$ time series across all cases, for $30 < Nt < 200$, the interval which is characterized by the emergence of stratified turbulence and the subsequent transition into the Q2D regime.

### 5.4. *'Stratified turbulence' diagnostics*

Having quantified the dependence of buoyancy-driven shear on $Re$ and $Fr$, one may now assess its ability to generate Kelvin–Helmholtz instabilities by examining the local Richardson number $Ri_{loc}$:

$$Ri_{loc} = \frac{\dfrac{-g}{\rho_0}\dfrac{\partial \rho_T}{\partial z}}{\left(\dfrac{\partial u}{\partial z}\right)^2 + \left(\dfrac{\partial v}{\partial z}\right)^2}, \tag{5.3}$$

where $\rho_T(x, y, z, t) = \overline{\rho}(z) + \rho'(x, y, z, t)$. Figure 16 contrasts contours of $|Ri_{loc}|$ on the $Oxz$ centreplane between runs R5F4 and R100F4 at time $Nt = 30$. In the low-$Re$ case, there are very few bands of $|Ri_{loc}| < 1$ with a near-negligible number of regions of $|Ri_{loc}| < 1/4$, where shear instability is likely. Any such regions rapidly disappear at subsequent times. The high-$Re$ simulation, however, shows a proliferation of streaks with $|Ri_{loc}| < 1/4$, which are concentrated along the planes of maximum vertical shear.

Figure 17 shows the time series of $Ri_H$, which is the average of the horizontally averaged values of $Ri_{loc}$ at each of the two planes of maximum vertical shear (Hebert & de Bruyn Kops 2006). RdBK recommend $Ri_H < 1$ as an approximate criterion for secondary instabilities and turbulence to develop on average throughout the flow. All low-$Re$ curves cross this threshold value at $Nt = 10$, when buoyancy has not yet had the chance to organize the vorticity field into horizontal layers. In contrast, the high-$Re$ curves collapse across all $Fr$ and exceed the critical value of $Ri_H$ at some point in the interval $100 < Nt < 200$, an observation consistent with the persistence of secondary instabilities shown in figures 10 and 11.

As proposed independently by the scaling arguments of RdBK and Billant & Chomaz (2001), a criterion equivalent to $Ri_H < 1$ for the development of shear instability, and therefore stratified turbulence, is $Re_H Fr_H^2 > 1$, where $Re_H$ and $Fr_H$ are appropriately defined local horizontal Reynolds and Froude numbers, respectively. Specifically, $Re_H \equiv u_H l_H/\nu$ and $Fr \equiv u_H/(l_H N)$. In this study, the characteristic horizontal velocity $u_H$ and horizontal length scale $l_H$ are computed through a slight

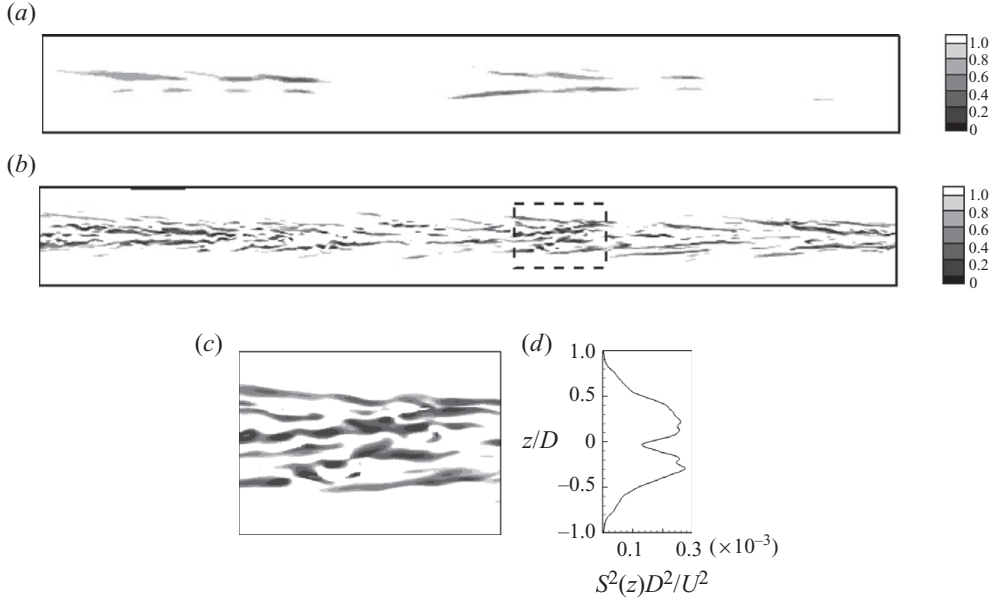(*a*)



(*b*)



(*c*)

(*d*)

FIGURE 16. Contour plots at $Nt = 30$ of the absolute value of the local Richardson number, $|Ri_{loc}|$, on a $26\frac{2}{3}D \times 2D$ subsection of the $Oxz$ centreplane. (*a*) R5F4 and (*b*) R100F4. (*c*) A zoomed view of the region delineated by the dashed line in (*b*). (*d*) Profile of mean square vertical shear at that time (as also shown in figure 14).
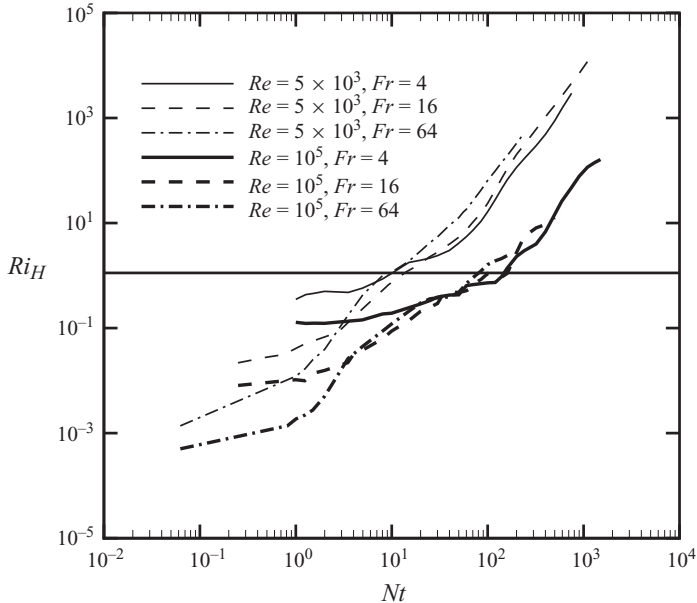


FIGURE 17. Evolution of the wake volume-averaged local Richardson number, $Ri_{loc}$.

variation of the procedure outlined by Hebert & de Bruyn Kops (2006). Based on the decomposition of (3.1) and the premise that the quasi-horizontal motions driving the vertical shear originate from perturbations to the mean flow, $u_H$ is defined as the average of the r.m.s. values of horizontal fluctuating velocity computed over the
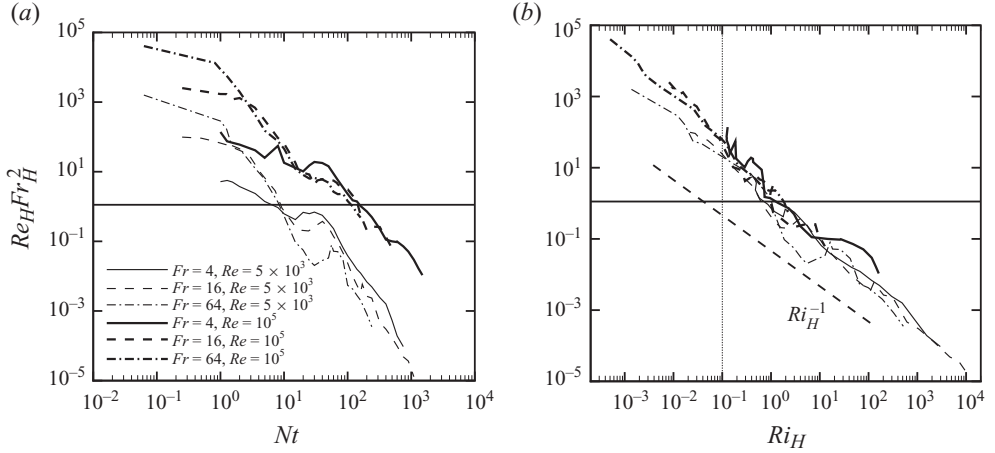
FIGURE 18. (*a*) Evolution of $Re_H Fr_H^2$. (*b*) $Re_H Fr_H^2$ as a function of $Ri_{loc}$. The dashed line represents the $-1$ power law observed by Hebert & de Bruyn Kops (2006).

two planes of maximum vertical shear. The length scale, $l_H$, is computed from the zero-crossing of the autocorrelation function:

$$R(r) = \frac{1}{2} \frac{\langle u'(x+r)u'(x)\rangle_H}{\langle u'\rangle_H} + \frac{1}{2} \frac{\langle \omega_z(y+r)\omega_z(y)\rangle_H}{\langle \omega_z\rangle_H}, \quad (5.4)$$

with

$$l_H = r \quad \text{for} \quad R(r) = 0. \quad (5.5)$$

The first term on the right-hand side of (5.4) represents the autocorrelation of the fluctuating streamwise velocity $u'$ in the $x$-direction and the second term represents the autocorrelation of the vertical vorticity $\omega_z$ in the $y$-direction. The subscript $H$ represents averaging of the streamwise and spanwise autocorrelations over the planes of maximum vertical shear. Computation of the $x$-autocorrelation necessitates removal of the mean velocity whose $x$-independence precludes the presence of a zero-crossing in the correlation function. At a given $x$-location, on account of the influence of the mean flow, the $v$-velocity tends to maintain a fixed sign in the transverse direction. Thus, $\omega_z$ enables a more reliable estimate of the $y$-autocorrelation.

Figure 18(*a*) shows the evolution of $Re_H Fr_H^2$ for all cases. The characteristic horizontal velocity, $u_H$, and length scale, $l_H$, evolve to maintain a near-constant value of $Re_H$ throughout the entire simulation, in agreement with Hebert & de Bruyn Kops (2006). Note that $Re = 5 \times 10^3$ and $10^5$ have $Re_H \approx 100$ and $2 \times 10^4$, respectively. For all cases, $Fr_H$ quickly drops below unity at $Nt \approx 2$ and continues to decrease steadily with all curves collapsing for $Nt > 10$. Thus, the development of $Re_H Fr_H^2$ in time is set by the initial value of $Re_H$. Figure 18 shows that $Re_H Fr_H^2 > 1$ holds for the low-$Re$ data only up to $Nt \approx 10$. In contrast, $Re_H Fr_H^2 > 1$ for all high-$Re$ runs until $Nt \approx 200$, in agreement with figure 17. Moreover, as in the high-$Re$ time series in figure 17, $Re_H Fr_H^2$ curves appear to collapse for $Nt > 10$ at high $Re$. The one-to-one correspondence in the occurrence of critical value transitions in figures 18(*a*) and 17 suggests that, in accordance with the original scaling arguments of RdBK, $Re_H Fr_H^2 \approx Ri_H^{-1}$, which appears to be confirmed by figure 18(*b*). Excluding all points with $Ri_H < 0.1$, which correspond primarily to the 3D regime where non-stratified
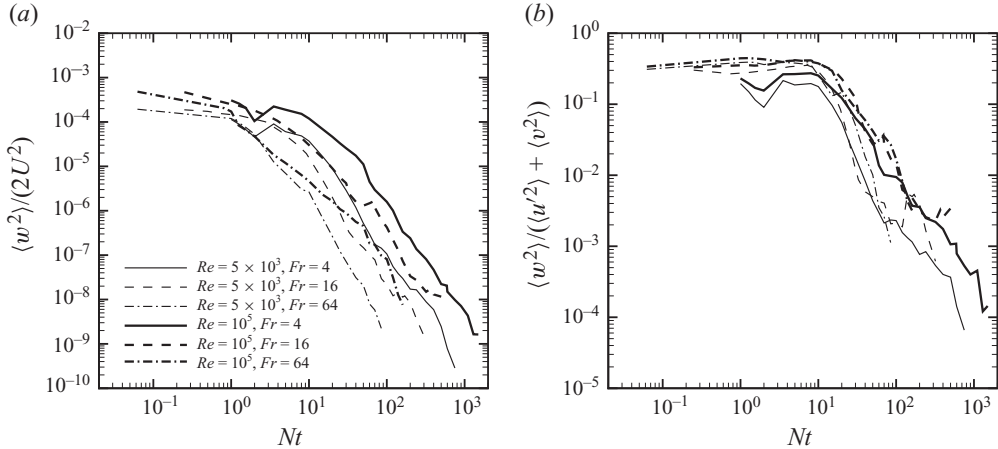
FIGURE 19. (*a*) Evolution of the wake volume-averaged vertical kinetic energy. (*b*) Same quantity but normalized by the wake volume-averaged horizontal kinetic energy.

dynamics dominate, a least-squares fit of $Fr_H Re_H^2 \approx Ri_H^\alpha$ yields an average exponent for all six cases of $\alpha = 1.18 \pm 0.05$.

These results further support the suggestion of Hebert & de Bruyn Kops (2006) that $Re_H Fr_H^2$ provides a reliable estimate for the local Richardson number and may be therefore used as an alternative indicator for stratified turbulence when only horizontal but no vertical measurements are available. Note also that the use of $U_0$ (or the horizontally averaged value of the total instantaneous horizontal velocity) and $L_H$ as characteristic horizontal velocity and length scales, respectively, is found to significantly overestimate both $Re_H$ and $Fr_H$ in such a way that $Re_H Fr_H^2 = 1$ is observed at a time which is long after any secondary events have occurred in the flow.

## 5.5. *Vertical kinetic energy of the intermediate-to-late-time wake*

The enhanced buoyancy-driven vertical shear and resulting secondary instabilities and turbulence of the high-$Re$ wakes are expected to be associated with enhanced vertical velocities and isopycnal overturning. Figure 19(*a*) provides further evidence for the above behaviour in high-$Re$ stratified wakes, which shows the evolution of the average vertical kinetic energy, $\langle w^2 \rangle / 2$, integrated over the wake volume (as defined by the rectangular volume on the wake centred with a cross-section of $[-2L_H, 2L_H] \times [-2L_V, 2L_V]$). For $30 < Nt < 100$, at a given $Fr$, the vertical kinetic energy of a high-$Re$ wake is a factor of 8–15 greater than that of its low-$Re$ counterpart.

In figure 19(*b*), $\langle w^2 \rangle / 2$ is normalized by the wake-integrated horizontal fluctuating kinetic energy $\langle u'^2 \rangle / 2 + \langle v^2 \rangle / 2$, which, in agreement with RdBK, is found to have only a weak dependence on $Re$. At each $Re$, the normalized curves collapse quite well across different $Fr$. Upon completion of relaxation (not shown here), the ratio $\langle w^2 \rangle / (\langle u'^2 \rangle + \langle v^2 \rangle)$ is exactly equal to $1/2$, corresponding to equipartition of kinetic energy across all three components (see §3.2). The time series of figure 19(*b*) are sampled as soon as the transition run has ended. At this point, although $\langle w^2 \rangle / \langle v^2 \rangle$ is very close to unity, $\langle w^2 \rangle / \langle u'^2 \rangle$ lies in the range of $[0.3, 0.8]$, as it is likely that significant production of streamwise velocity fluctuations has occurred during the transition run. The $Fr = 4$ cases showed the lowest values of $\langle w^2 \rangle / \langle u'^2 \rangle$, presumably

due to the stronger effect of stratification during the transition run. The initiation of the decay of $\langle w^2 \rangle / (\langle u'^2 \rangle + \langle v^2 \rangle)$ at $Nt \approx 10$ is consistent with the experimental observations of Sp02 (see his figure 12$b$).

In the high-$Re$ wakes, for $30 < Nt < 200$, $\langle w^2 \rangle / (\langle u'^2 \rangle + \langle v^2 \rangle)$ can be as much as 20 times larger than the corresponding low-$Re$ value. Nonetheless, $\langle w^2 \rangle / (\langle u'^2 \rangle + \langle v^2 \rangle)$ lies in the range of $[0.003, 0.05]$, suggesting that the vertical motions associated with secondary events may not contribute significantly to overall wake dynamics. Such an argument is likely to be weakened with increasing $Re$, as the enhancement of buoyancy-driven shear would provide for more vigorous (and possibly more space-filling) secondary instabilities and ensuing turbulence.

## 6. Discussion

### 6.1. *Reynolds and Froude number scaling*

The $Re/Fr^2$ scaling identified in §5.3 and figure 15($b$) may be interpreted as follows. Although stronger stratification is commonly associated with enhanced suppression of vertical motion, it provides for enhanced vertical shear in the intermediate-to-late wake, as it biases the flow towards stronger vertical velocity gradients (Fincham *et al.* 1996; Diamessis & Nomura 2000). At lower $Re$, viscosity diminishes the magnitude of the vertical shear which is distributed over layers of a greater thickness and has a considerably slower growth rate of the Kelvin–Helmholtz instability. Moreover, the weaker shear is responsible for higher values of the local Richardson number and reduced potential for secondary instabilities (see §5.4). In the same vein, although case R5F4 has comparable and even stronger shear than the high-$Re$ runs at $Fr = 16$ and 64 (figure 15$b$), the latter two operate against a noticeably weaker stratification and can therefore support secondary instabilities. Finally, at a fixed $Re$, the weaker shear magnitude observed with increasing $Fr$ may be attributed to having viscosity operating over a longer window (in $x/D$) within the wake core before buoyancy can establish a layered structure.

Given the collapse of all $Re_H Fr_H^2$ curves at a given $Re$ for $Nt > 10$ (figure 18$a$) and the scaling of the mean-squared shear with $Re$ (figure 15$b$), it is reasonable to expect that the critical value of $Ri_H$ (and, therefore, $Re_H Fr_H^2$) will be attained at later times with increasing $Re$, i.e. *secondary instabilities and turbulence will persist for an even longer time*. Thus, at a given $Nt$ during the NEQ regime, higher $Re$ will correspond to lower values of $Ri_H$. In this case, the enhanced shear will provide for more vigorous and possibly more space-filling secondary events, which may establish even higher levels of vertical kinetic energy than those shown in figure 19.

The collapse of the high-$Re$ $Re_H Fr_H^2$ time series for $Nt > 10$ (figure 18$a$) merits further discussion. First, it indicates that at a given sufficiently high $Re$, the turbulence inside a stratified wake self-organizes in such a way that it evolves in an $Fr$-independent manner throughout the entire NEQ regime. Such behaviour should hold for other strongly stratified turbulent flows near or within the inviscid limit and is directly linked to the theoretical predictions of self-similarity of Billant & Chomaz (2001). Note that multiplying the vertical axis of figure 18($a$) with $1/Re$ yields only a partial collapse of the time series. Thus, further analysis is required to determine the high-$Re$ scaling of the $Re_H Fr_H^2$ time series. Such a scaling would enable the construction of a universal curve for $Re_H Fr_H^2(Nt)$ and the exact determination of its unity-crossing point as a function of $Re$ and $Fr$.

Hebert & de Bruyn Kops (2006) have shown that $Re_H Fr_H^2$ is equivalent to the buoyancy Reynolds number, $Re_b = \epsilon / (\nu N^2)$, a quantity commonly used in the

oceanographic literature as a measure of the scale separation between the largest (Ozmidov) and smallest (Kolmogorov) scales (Ivey & Imberger 1991). The collapse of the $Re_H Fr_H^2$ times series at high $Re$ in the NEQ regimes indicates that, at a particular value of $Nt$, this scale separation is independent of $Fr$ and the turbulent kinetic energy dissipation rate is set by $N^2$, i.e. the stratification.

### 6.2. *Universality of secondary events and fine structure disappearance*

A characteristic signature of the secondary instabilities and turbulence is the fine structure embedded within a larger-scale background vortical motion (figure 8). As indicated in §5.2, a similar signature has been observed in a number of simulations of other high-$Re$ strongly stratified flows with more idealized initial conditions (Waite & Bartello 2003; Brethouwer *et al.* 2007; Deloncle *et al.* 2008). This similarity suggests that this type of vorticity field structure is a universal feature of highReynolds-number stratified flows, regardless of the exact initial conditions. All that is required is the presence of a strong vortical mode (Riley & Lelong 2000) that is either inherent in the initial condition (Waite & Bartello 2003) or develops naturally during the flow evolution, as is the case with a stratified wake.

Curiously enough, however, this type of fine structure is not observed within the pancake vortices reproduced by the $Re = 10^5$ wake simulations of Dommermuth *et al.* (2002), with the pancakes showing a visibly diffuse structure as early as $Nt = 50$. Such behaviour may be attributed to the enhanced artificial dissipation of their SGS model and the reduced resolution in the vertical direction of the particular study (see §4). On the contrary, in the high-$Re$ simulations presented here, the fine structure disappears at much later times. Specifically, the fine structure vanishes by $Nt \approx 300$, 160 and 70 for $Fr = 4$, 16 and 64, respectively, times which are quite close to when $Re_H Fr_H^2 \approx 1$.

### 6.3. *Self-similarity modelling of high-Reynolds-number stratified wakes*

The observations of high vertical kinetic energy focused in spatio-temporally intermittent bursts of turbulence in the mid-to-late-time stratified wake suggest that the assumption of Meunier *et al.* (2006) of zero vertical transport in a stratified wake for $Nt \geqslant 2$ may be too stringent for sufficiently high $Re$. Whereas the condition $Fr_{H,m} = U_0/(L_H N) \approx 1$ (where $Fr_{H,m}$ is a horizontal Froude number defined through the mean profile) does indeed signal the onset of the NEQ regime, it does not automatically correspond to suppression of vertical transport. A more accurate condition for the onset of this suppression would be $Re_H Fr_H^2 = 1$, adjusted by a multiplicative factor if mean velocities and length scales are used (see §5.4).

### 6.4. *Implications for the field: intermittency and horizontal spectra*

The spatio-temporal intermittency of the secondary instabilities and turbulence additionally suggests that a similar process may be responsible for the episodic nature of turbulent events in the stratified open ocean (Thorpe 2005). Observations of turbulent microstructure in an environment with strong background shear (Itsweire, Osborn & Stanton 1989) may correspond to secondary bursts feeding off the mean shear of a larger-scale original event (which from its onset, or subsequently in its evolution, is associated with a strong vortical mode), as is the case here. In a similar geophysical context, the decade-wide $k_x^{-5/3}$ inertial range seen in the mid-to-late-time streamwise kinetic energy spectra of stratified wakes (figure 5), also reported by RdBK and Brethouwer *et al.* (2007) (who both, nevertheless, used more idealized initial conditions), is directly linked to buoyancy-driven secondary instabilities and turbulence which drive a Kolmogorov-like forward energy cascade in strongly stratified high-$Re$ turbulent flows (Linborg 2006). The observation of this

spectral signature in a localized canonical flow with turbulent initial conditions, such as a towed-body wake (more evolved variants of which are common in the ocean and atmosphere, as discussed in §1.1), provides additional support to the claims of Riley & Lindborg (2008). Specifically, they suggest that stratified turbulence may be the physical process underlying a number of observations of $-5/3$ horizontal spectral slope in the ocean and atmosphere, where the turbulence is presumed to be organized in highly oblong layers (much like the geometry of the wake in the NEQ regime) extending over $O(10\,\mathrm{km})$ to $O(100\,\mathrm{km})$ in the horizontal.

### 6.5. *Vertical transport in a localized stratified turbulent flow*

At sufficiently high initial Reynolds numbers, the original turbulence is not completely suppressed by buoyancy but is partially reactivated through the buoyancy-enhanced vertical shear. If indeed the secondary turbulence persists up to $Nt \approx O(10^3)$ from the formation of the original turbulent event, the implications for estimating vertical transport coefficients are significant. A preliminary analysis of the high-$Re$ data sets considered here (Diamessis 2010) has shown that the wake-averaged vertical Reynolds stress magnitude scales with the corresponding wake-averaged horizontal turbulent kinetic energy. Furthermore, vertical eddy viscosities computed at high $Re$ on the planes of maximum vertical shear (figure 14) are almost 10 times larger than their molecular counterpart at $Nt = 30$, when all vertical motions and turbulent transport are commonly expected to have fully subsided. At even higher $Re$, based on the discussion of §6.1 on the expected enhancement of the associated buoyancy-driven shear and resulting turbulence, the ratio of vertical viscosity to its molecular counterpart is likely to have even larger values and to persist well above unity at much later times.

## 7. Concluding remarks

Spectral multi-domain-based implicit LES of the stratified turbulent wake of a towed sphere have revealed a significant dependence of wake similarity scaling and underlying flow structure on the sphere-based Reynolds number, $Re$. As $Re$ is increased, a distinct prolongation of the NEQ regime takes place, as evidenced by the persistence time of slower decay rates of the mean wake kinetic energy. As the mean wake height remains near constant, the wake continues to expand in the horizontal, establishing a more oblique wake cross-section. Within the wake core, buoyancy drives the development of quasi-horizontal motions and the reorganization of the original three-dimensional turbulent vorticity field into distinct horizontal layers with strong vertical shear. The strength of these pronounced shear layers increases with $Re$, whereas their thickness is reduced, leading to higher susceptibility to Kelvin–Helmholtz instability. Somewhat counterintuitively, the tendency towards shear instability is enhanced with decreasing internal Froude number, $Fr$ (for any value of $Fr \geqslant 4$). At $Re = 10^5$, the persistent secondary instabilities and resulting turbulence survive until $Nt \approx 100$ and can drive significant vertical motions, leading to over-turning at times when buoyancy is commonly expected to have fully suppressed the original turbulence. The strength of the buoyancy-driven vertical shear sustaining the secondary instabilities and turbulence scales as $Re/Fr^2$. This scaling along with the description of the state of the stratified turbulence in the NEQ regime at a given high $Re$ by an $Fr$-independent $Re_H Fr_H^2$ curve ($Re_H$ and $Fr_H$ are turbulent horizontal Reynolds and Froude numbers, respectively) enables the prediction of the strength and persistence time of these secondary motions. Although the secondary

events appear to be intermittently embedded within larger-scale vortical modes, the emergence of diffuse pancake vortices, similar to those observed in previous low-$Re$ experiments, is significantly delayed with increasing $Re$. This is the first systematic observation and characterization of such secondary events in a controlled laboratory or numerical experiment with a realistic turbulent initial condition.

At their core, the results presented here motivate a re-examination of the commonly perceived life cycle of a localized stratified turbulent patch. Furthermore, the presence of a persistent highly energetic NEQ regime (lasting up to $Nt \approx O(10^3)$ or even longer at geophysical values of $Re$) that intervenes between the 3D and Q2D regimes is very likely to stimulate a reconsideration of the existing parametrizations of stratified turbulence and mixing in the ocean and atmosphere and an alternative interpretation of spectra sampled in the field. Finally, from a naval hydrodynamics standpoint, significant implications arise in terms of the long-time signature of submerged body wakes and the formulation of relevant predictive modelling tools.

## Appendix A. Setting the initial wake length scales/velocities

To allow for a fully three-dimensional initial flow field that transitions smoothly into the NEQ regime for all $Fr \in [4, 64]$, this study seeks a choice of characteristic wake length and velocity scales in (3.2) and (3.3) that reliably approximate the near wake at $x/D = 2$. Beyond this point, the mean wake should transition into a self-similar evolution by $x/D = 6$, as indicated by the experiments of Bevilaqua & Lykoudis (1978). Thus, for all $Fr$ values under consideration, self-similar behaviour throughout almost the entire the NEQ regime should be expected.

No descriptions are available from past numerical simulations on the structure of the near-wake mean and fluctuating velocity profiles at the $Re$ values of interest. However, laboratory data for the near wake are limited to one-dimensional profiles of $U_X$ and $u'_x$ obtained from hot-wire transects through the wake centreline as close as $x/D = 0.236$ to the body (Bevilaqua & Lykoudis 1978). By assuming axisymmetry and energy equipartition across all fluctuating velocity components, one may introduce the Bevilaqua & Lykoudis data into (3.2) and (3.3) to set up initial mean and fluctuating flow fields for the simulations. Nonetheless, when implementing such initial flow fields with a value of $u_0/U_0 = 0.4$ (as chosen by Dommermuth *et al.* 2002) in the spectral multi-domain penalty method solver, self-similar evolution of the mean flow was found to be spuriously delayed until $x/D \approx 40$. Reduction of $u_0/U_0$ by as much as a factor of four did not accelerate the emergence of self-similar behaviour.

Restarting the simulation upon the sudden termination of the relaxation procedure does constitute an impulsively started problem, i.e. the numerical solution is essentially shocked. Since the mean and fluctuating profiles are abruptly allowed to evolve,

transients will develop. Spectral schemes are particularly sensitive to such transients, in part due to their higher accuracy and minimal and explicitly controlled artificial dissipation. Non-Fourier higher-order element-based schemes have been found to be even more sensitive to initialization transients in impulsively started stratified flow processes, particularly when the initial condition is not an exact solution of the Navier–Stokes equations (Abdilghanie & Diamessis 2011), with the transients often persisting for very long times. In the specific flow under consideration, the initial mean wake profile, constructed by assuming axisymmetry of the one-dimensional transects of Bevilaqua & Lykoudis (1978), does not satisfy conservation of momentum as prescribed by Meunier *et al.* (2006) and, therefore, is not a solution of the incompressible Navier–Stokes equations. Thus, the observed emergence of an excessively long adjustment until the onset of self-similar behaviour is not unexpected in a simulation with the particular spectral multi-domain scheme.

An alternative prescription of the near-wake mean flow is sought to minimize the transition to self-similar evolution. We therefore assume a self-similar wake as early as $x/D = 2$ and select mean and fluctuating velocity profiles prescribed by the relevant theory at this location (Tennekes & Lumley 1972; Meunier *et al.* 2006). This assumption may be justified by this study's focus: the reproduction of realistic behaviour upon entry into the NEQ regime and thereafter, and not details of the near wake.

The expressions for the width/height and centreline velocity of a self-similar unstratified wake at a given downstream distance $x/D$ are readily given by Meunier *et al.* (2006):

$$L_H = L_V = D_m \left( \frac{3x}{8 R_3 D_m} \right)^{1/3}, \tag{A 1}$$

$$U_0 = \frac{U}{8} \left( \frac{3x}{8 R_3 D_m} \right)^{-2/3}, \tag{A 2}$$

where $R_3$ is a turbulent Reynolds number and $D_m = D\sqrt{C_D/2}$ is defined as a momentum thickness based on the drag coefficient of the body $C_D$. The values chosen here are $R_3 = 4$ (Bevilaqua & Lykoudis 1978) and $C_D = 0.4$ (Meunier & Spedding 2004).

No value for $u_0/U_0$ is given in Gourlay *et al.* (2001), and Dommermuth *et al.* (2002) do not justify their choice of a value of 0.41, although it is very close to the value measured by Bevilaqua & Lykoudis (1978). It is also possible that both of these investigations did not focus on the sensitivity of the numerical results to $u_0/U_0$ as it may have been regarded as inconsequential to the evolution of the intermediate-to-late wake. The expectation that the initial condition will rapidly adjust into the intermediate wake behaviour no matter what the choice of $u_0/U_0$ is not totally unreasonable. Note, however, that the wake's shear-layer profile is convectively unstable and any amplified disturbance (as represented in an excessively high value of $u_0/U_0$) in the near wake may persist for significant distances downstream (L. Redekopp, personal communication, 2005). A spectral/spectral-multi-domain solver, such as that used in this study, is most liable to faithfully reproduce the downstream persistence of any artificially amplified near-wake disturbances.

Nevertheless, spectral multi-domain LES initialized with mean wake velocity profiles given by (A 1) and (A 2) were not found to yield a self-similar mean flow immediately upon the termination of relaxation. Although the onset of mean flow self-similarity

was accelerated compared to the previous choice of initial mean profile, it was still not observed until $8 < x/D < 20$, the delay increasing with increasing values $u_0/U_0$ (chosen in the range of $[0.1, 0.4]$). Furthermore, fluctuations with $u_0/U_0 < 0.1$ were not energetic enough to become correlated with the mean flow.

Insight into the sensitivity to the choice of $u_0/U_0$ may be gained from the laboratory study of Browand & Latigo (1979), who examined the growth rates of a two-dimensional shear layer for different levels of turbulence on the top side of the splitter plate. A turbulent top boundary layer delayed the transition to self-similar growth as compared with the case of laminar flow over the splitter plate. The delay was proportional to the levels of turbulent kinetic energy. A possible cause for this transition was conjectured to be the interaction of the coherent structures inside the turbulent boundary layer with those characteristic of a monochromatically driven Kelvin–Helmholtz instability (e.g. billows and braids, Thorpe 2005). Since self-similarity theory works with a reduced set of equations that does not take into account the coherent structure that destabilizes the mean flow profile of (3.3), a similar mechanism may be operative in the wake simulations considered here.

For the production runs described here, to minimize any lag in the onset of self-similarity, the value of $u_0/U_0 = 0.1$ is chosen. This value is equal to that measured by Bevilaqua & Lykoudis (1978) at $x/D = 2$. It is also very close to the asymptotic value of 0.16 observed in all the Browand & Lattigo experiments at $O(400)$ integral thicknesses from the splitter plate, when self-similarity was well-established in the evolution of the mean shear-layer velocity profile . The choice of $u_0/U_0 = 0.1$ is found to produce well-correlated fluctuating and mean wake flow fields that become self-similar in the mean by $x/D = 8$. Thus, another preliminary run, the 'transition run', operating within the interval $2 < x/D < 8$, follows the relaxation run (see also §3).

It is at the end of the transition run that the main run begins. However, $U_0$ and $L_H$ change during the transition run, leading to an inevitable reduction of local Reynolds and Froude numbers, $Re_L = U_0 L_H / \nu$ and $Fr_L = 2U_0/(L_H N)$, from their original values at the end of relaxation. If these values of $Re_L$ and $Fr_L$ are chosen to represent a near wake presumed to be axisymmetric at $x/D = 2$, this wake will correspond to lower values of $Re$ and $Fr$ than those originally intended.

To compensate, the value of $U_0$ used during relaxation is set to be 50 % larger than that given by (A 2) for $x/D = 2$. The resulting values of $Re_L$ and $Fr_L$ at the end of transition differ by only 5 % from their self-similar counterparts for the $Re$ and $Fr$ of interest at $x/D = 2$.

## Appendix B. Initial wake density field

Beyond the involved process of prescribing the characteristics of the initial mean wake velocity profile, an additional effort is required towards designating a physically realistic density field. Gourlay *et al.* (2001) and Brucker & Sarkar (2010) assumed zero density perturbations at the beginning of their stratified wake simulations and the same assumption was made by Dommermuth *et al.* (2002) for the density field upon the termination of relaxation. Such a choice of an initial density field was justified in both studies based on the assumption that the particular details of the initial density field are inconsequential to the evolution of the intermediate-to-late-time wake.

However, the near wake will clearly drive significant isopycnal stirring and overturning until $x/D = 2$. Superimposing an unperturbed stable density stratification on a velocity field approximating the near wake at $x/D = 2$ may once again be

regarded as an impulsively started problem, where the velocity field is shocked with an externally imposed stratification. Such an approach has typically been used in DNS of stratified homogeneous turbulence (Jacobitz, Sarkar & Van Atta 1997) and no issues with detrimental transients have been reported (Diamessis & Nomura 2004). When this approach was used with the spectral multi-domain solver, the solution was contaminated by re-stratification-related transients whose most visible signatures were distinct unphysical oscillations in the wake height with amplitudes which increased with decreasing $Fr$ and persisted as late as $Nt \approx 50$ for $Fr = 4$. Motivated by the work of Gerz & Yamazaki (1993), an effort to seed the initial density field with either random fluctuations or fluctuations generated during the relaxation procedure by turbulent stirring of the isopycnals – the length scale of the fluctuations set in both cases as some prescribed percentage of $L_V$ – produced even stronger oscillations in $L_V$.

Given the sensitivity of the spectral multi-domain solver to any unrealistic assumptions about the initial condition, a transient-free approach was devised that generates density fluctuations that develop in confluence with the velocity field. The specific approach was based on the conceptual construct of the wake of a fixed body in a free stream, where the stratification is gradually ramped-up downstream to the desired value. In analogy, in the simulations discussed here, during the transition run, the value of the mean density gradient $d\bar{\rho}/dz$ in (2.3) is ramped-up in a time with a half-Gaussian until it reaches its maximum value at the end of this preliminary run. This approach was found to nearly eliminate all re-stratification-related transients and the evolution of $L_V$ was found to agree well with the observations of Sp02.

## REFERENCES

ABDILGHANIE, A. M. & DIAMESSIS, P. J. 2011 On the generation and evolution of numerically simulated large amplitude internal gravity wave packets. *Theor. Comput. Fluid Dyn.* (in press).

BEVILAQUA, P. M. & LYKOUDIS, P. S. 1978 Turbulence memory in self-preserving wakes. *J. Fluid Mech.* **89**, 589–606.

BILLANT, P. & CHOMAZ, J. M. 2000a Experimental evidence for a new instability of a vertical columnar vortex pair in a strongly stratified fluid. *J. Fluid Mech.* **418**, 167–188.

BILLANT, P. & CHOMAZ, J. M. 2000b Theoretical analysis of the zigzag instability of a vertical columnar vortex pair in a strongly stratified fluid. *J. Fluid Mech.* **419**, 29–63.

BILLANT, P. & CHOMAZ, J. M. 2001 Self-similarity of strongly stratified inviscid flows. *Phys. Fluids* **13** (6), 1645–1651.

BOGEY, C. & BAILLY, C. 2006 Computation of a high-Reynolds-number jet and its radiated noise using large eddy simulation based on explicit filtering. *Comput. Fluids* **35** (10), 1344–1358.

BONNETON, P., CHOMAZ, J. M. & HOPFINGER, E. J. 1993 Internal waves produced by the turbulent wake of a sphere moving horizontally in a stratified fluid. *J. Fluid Mech.* **254**, 23–40.

BONNIER, M. & EIFF, O. 2002 Experimental investigation of the collapse of a turbulent wake in a stratified fluid. *Phys. Fluids* **14** (2), 791–801.

BORIS, J. P., GRINSTEIN, F. F., ORAN, E. S. & KOLBE, R. L. 1992 New insights into large eddy simulation. *Fluid Dyn. Res.* **10**, 199–228.

BOYD, J. P. 2001 *Chebyshev and Fourier Spectral Methods*. Dover.

BRETHOUWER, G., BILLANT, P., LINDBORG, E. & CHOMAZ, J. M. 2007 Scaling analysis and simulation of strongly stratified turbulent flows. *J. Fluid Mech.* **585**, 343–368.

BROWAND, F. K., GUYOMAR, D. & YOON, S. C. 1987 The behaviour of a turbulent front in a stratified fluid: experiments with an oscillating grid. *J. Geophys. Res.* **92**, 5329–5341.

BROWAND, F. K. & LATIGO, B. O. 1979 Growth of the two-dimensional mixing layer from a turbulent and non-turbulent boundary layer. *Phys. Fluids* **22** (6), 1011–1019.

BRUCKER, K. A. & SARKAR, S. 2010 A study of momentumless wakes in stratified fluids. *J. Fluid Mech.* **652**, 373–404.

Chomaz, J. M., Bonetton, P., Butet, A. & Hopfinger, E. J. 1993*a* Vertical diffusion of the far wake of a sphere moving in a stratified fluid. *Phys. Fluids* **5** (11), 2799–2806.

Chomaz, J. M., Bonetton, P., Butet, A. & Perrier, M. 1992 Froude number dependence of the flow separation line on a sphere towed in a stratified fluid. *Phys. Fluids* **4** (2), 254–258.

Chomaz, J. M., Bonetton, P. & Hopfinger, E. J. 1993*b* The structure of the near wake of a sphere moving in a stratified fluid. *J. Fluid Mech.* **254**, 1–21.

Cook, A. W. & Cabot, W. H. 2005 Hyperviscosity for shock-turbulence interactions. *J. Comput. Phys.* **203**, 379–385.

Cousin, L. & Pasquetti, R. 2004 High-order methods for the simulation of transitional to turbulent wakes. In *Advances in Scientific Computing and Applications* (ed. T. Tang, Y. Lu & W. Sun), pp. 133–143. Sciences Press.

Deloncle, A., Billant, P. & Chomaz, J. M. 2008 Nonlinear evolution of the zigzag instability in stratified fluids: a shortcut on the route to dissipation. *J. Fluid Mech.* **599**, 229–239.

Diamessis, P. J. 2010 Vertical transport in high-Reynolds-numbers stratified turbulent wakes. In *Sixth International Symposium on Environmental Hydraulics*. Athens, Greece.

Diamessis, P. J., Domaradzki, J. A. & Hesthaven, J. S. 2005 A spectral multidomain penalty method model for the simulation of high-Reynolds-number localized stratified turbulence. *J. Comput. Phys.* **202**, 298–322.

Diamessis, P. J., Lin, Y. C. & Domaradzki, J. A. 2008 Effective numerical viscosity in spectral multidomain penalty method-based simulations of localized turbulence. *J. Comput. Phys.* **227**, 8145–8164.

Diamessis, P. J. & Nomura, K. K. 2000 Interaction of vorticity, rate-of-strain and scalar gradient in stratified homogeneous sheared turbulence. *Phys. Fluids* **12**, 1166–1688.

Diamessis, P. J. & Nomura, K. K. 2004 The structure and dynamics of overturns in stably stratified homogeneous turbulence. *J. Fluid Mech.* **499**, 197–229.

Diamessis, P. J. & Spedding, G. R. 2006 Scaling and structure of stratified turbulent wakes at high Reynolds numbers. In *Sixth International Symposium on Stratified Flows*, pp. 183–188. Perth, Australia.

Domaradzki, J. A., Loh, K. C. & Yee, P. P. 2002 Large eddy simulations using the subgrid-scale estimation model and truncated Navier–Stokes dynamics. *Theor. Comput. Fluid Dyn.* **15**, 421–450.

Dommermuth, D. G., Rottman, J. W., Innis, G. E. & Novikov, E. A. 2002 Numerical simulation of the wake of a towed sphere in a weakly stratified fluid. *J. Fluid Mech.* **473**, 83–101.

Fincham, A., Maxworthy, T. & Spedding, G. 1996 Energy dissipation and vortex structure in freely decaying, stratified grid turbulence. *Dyn. Atmos. Oceans* **23**, 155–169.

Gerz, T. & Yamazaki, H. 1993 Direct numerical simulation of buoyancy-driven turbulence in stably stratified fluid. *J. Fluid Mech.* **249**, 415–440.

Gibson, C. H. 1980 Fossil temperature, salinity and vorticity in the ocean. In *Marine Turbulence* (ed. J. C. T. Nihoul), pp. 221–258. Elsevier.

Gibson, C. H., Nabatov, V. & Ozmidov, R. 1993 Measurements of turbulence and fossil turbulence near Ampere Seamount. *Dyn. Atmos. Oceans* **19**, 175–204.

Godoy-Diana, R., Chomaz, J. M. & Billant, P. 2004 Vertical length scale selection for pancake vortices in strongly stratified viscous fluids. *J. Fluid Mech.* **504**, 229–238.

Gottlieb, D. & Hesthaven, J. S. 2001 Spectral methods for hyperbolic problems. *J. Comput. Appl. Maths* **128**, 83–131.

Gourlay, M. J., Arendt, S. C., Fritts, D. C. & Werne, J. 2001 Numerical modeling of initially turbulent wakes with net momentum. *Phys. Fluids* **13**, 3783–3802.

Grinstein, F. F. & Fureby, C. 2002 Recent progress on MILES for high-Reynolds-number flows. *Trans. ASME: J. Fluids Engng* **124**, 848–861.

Grinstein, F. F., Margolin, L. G. & Rider, W. J. 2007 *Implicit Large Eddy Simulation: Computing Turbulent Fluid Dynamics*. Cambridge University Press.

Hanazaki, H. 1988 A numerical study of three-dimensional stratified flow past a sphere. *J. Fluid Mech.* **192**, 393–419.

Harten, A., Engquist, B., Osher, S. & Chakravarthy, S. R. 1987 Uniformly high-order accurate essentially non-oscillatory schemes. Part III. *J. Comput. Phys.* **71**, 231–303.

Hebert, D. A. & de Bruyn Kops, S. M. 2006 Predicting turbulence in flows with strong stable stratification. *Phys. Fluids* **18**, 066602.

HESTHAVEN, J. S. 1997 A stable penalty method for the compressible Navier–Stokes equations: II. One-dimensional domain decomposition schemes. *SIAM J. Sci. Comput.* **18** (3), 658–685.

HESTHAVEN, J. S. & GOTTLIEB, D. 1996 A stable penalty method for the compressible Navier–Stokes equations: I. Open boundary conditions. *SIAM J. Sci. Comput.* **17** (3), 579–612.

ITSWEIRE, E. C., KOSEFF, J. R., BRIGGS, D. A. & FERZIGER, J. H. 1993 Turbulence in stratified shear flows: implications for interpreting shear-induced mixing in the ocean. *J. Phys. Oceanogr.* **23**, 1508–1522.

ITSWEIRE, E. C., OSBORN, T. & STANTON, T. 1989 Horizontal distribution and characteristics of shear layers in the seasonal thermocline. *J. Phys. Oceanogr.* **19**, 301–320.

IVEY, G. N. & IMBERGER, J. 1991 On the nature of turbulence in a stratified fluid. Part I. The energetics of mixing. *J. Phys. Oceanogr.* **21**, 650–658.

JACOBITZ, F. G., SARKAR, S. & VAN ATTA, C. W. 1997 Direct numerical simulations of the turbulence evolution in a uniformly sheared and stably stratified flow. *J. Fluid Mech.* **342**, 231–261.

KARAMANOS, G.-S. & KARNIADAKIS, G. E. 2000 A spectral vanishing viscosity method for large-eddy simulations. *J. Comput. Phys.* **163**, 22–50.

KARNIADAKIS, G. E., ISRAELI, M. & ORSZAG, S. A. 1991 High-order splitting methods for the incompressible Navier–Stokes equations. *J. Comput. Phys.* **97**, 414–443.

LAVAL, J. P., MCWILLIAMS, J. C. & DUBRULLE, B. 2003 Forced stratified turbulence: successive transitions with Reynolds number. *Phys. Rev.* E **68** (C2), 036308.

LILLY, D. K. 1983 Stratified turbulence and the mesoscale variability of the atmosphere. *J. Atmos. Sci.* **40**, 749–761.

LIN, J. T. & PAO, Y. H. 1979 Wakes in stratified fluids. *Annu. Rev. Fluid Mech.* **11**, 317–338.

LIN, Q., LINDBERG, W. R., BOYER, D. L. & FERNANDO, H. J. S. 1992 Stratified flow past a sphere. *J. Fluid Mech.* **240**, 315–354.

LINBORG, E. 2006 The energy cascade in a strongly stratified fluid. *J. Fluid Mech.* **550**, 207–242.

MAJDA, A. & GROTE, M. J. 1997 Model dynamics and vertical collapse in decaying strongly stratified flows. *Phys. Fluids* **9**, 2932–2940.

MEUNIER, P., DIAMESSIS, P. J. & SPEDDING, G. R. 2006 Self-preservation of stratified momentum wakes. *Phys. Fluids* **18**, 106601.

MEUNIER, P. & SPEDDING, G. R. 2004 A loss of memory in stratified momentum wakes. *Phys. Fluids* **16**, 298–303.

MINGUEZ, M., PASQUETTI, R. & SERRE, E. 2009 Spectral vanishing viscosity stabilized LES of the Ahmed body turbulent wake. *Commun. Comput. Phys.* **5**, 635–648.

MONKEWITZ, P. A. 1988 A note on vortex shedding from axisymmetric bluff bodies. *J. Fluid Mech.* **192**, 561–575.

ORSZAG, S. A. & PAO, Y. H. 1975 Numerical computation of turbulent shear flows. *Adv. Geophys.* **18** (1), 225–236.

OZGOKMEN, T. M., ILIESCU, T. & FISCHER, P. F. 2009 Large eddy simulation of stratified mixing in a three-dimensional lock-exchange system. *Ocean Model.* **26**, 134–155.

PAWLAK, G., MACCREADY, P., EDWARDS, K. A. & MCCABE, R. 2003 Observations on the evolution of tidal vorticity at a stratified deep water headland. *Geophys. Res. Lett.* **30** (24), 2234.

PRAUD, O. & FINCHAM, A. M. 2005 The structure and dynamics of stratified dipolar vortices. *J. Fluid Mech.* **544**, 1–22.

PRAUD, O., FINCHAM, A. M. & SOMMERIA, J. 2005 Decaying grid turbulence in a strongly stratified fluid. *J. Fluid Mech.* **522**, 1–33.

RILEY, J. J. & DE BRUYN KOPS, S. M. 2003 Dynamics of turbulence strongly influenced by buoyancy. *Phys. Fluids* **15**, 2047–2059.

RILEY, J. J. & LELONG, M. P. 2000 Fluid motion in the presence of strong stratification. *Annu. Rev. Fluid Mech.* **32**, 613–657.

RILEY, J. J. & LINDBORG, E. 2008 Stratified turbulence: a possible interpretation of some geophysical turbulence measurements. *J. Atmos. Sci.* **65** (7), 2416–2424.

ROTUNNO, R., GRUBISIC, V. & SMOLARKIEWICZ, P. K. 1999 Vorticity and potential vorticity in mountain wakes. *J. Atmos. Sci.* **56** (16), 2796–2810.

SAGAUT, P. 2002 *Large Eddy Simulation for Incompressible Flows: An Introduction*. Springer.

SENGUPTA, K., JACOBS, G. B. & MASHAYEK, F. 2009 Large-eddy simulation of compressible flows using a spectral-multidomain method. *Intl J. Numer. Meth. Fluids* **61** (3), 311–340.

SPEDDING, G. R. 1997 The evolution of initially turbulent bluff-body wakes at high internal Froude number. *J. Fluid Mech.* **337**, 283–301.

SPEDDING, G. R. 2001 Anisotropy in turbulence profiles of stratified wakes. *Phys. Fluids* **13** (8), 2361–2372.

SPEDDING, G. R. 2002 Vertical structure in stratified wakes with high initial Froude number. *J. Fluid Mech.* **454**, 71–112.

SPEDDING, G. R., BROWAND, F. K. & FINCHAM, A. M. 1996a The long-time evolution of the initially turbulent wake of a sphere in a stable stratification. *Dyn. Atmos. Oceans* **23**, 171–182.

SPEDDING, G. R., BROWAND, F. K. & FINCHAM, A. M. 1996b Turbulence, similarity scaling and vortex geometry in the wake of a towed sphere in a stably stratified fluid. *J. Fluid Mech.* **314**, 53–103.

SWEBY, P. K. 1984 High resolution schemes using flux limiters for hyperbolic conservation laws. *SIAM J. Numer. Anal.* **21**, 995.

TENNEKES, H. & LUMLEY, J. L. 1972 *A First Course in Turbulence*. MIT Press.

THORPE, S. A. 2005 *The Turbulent Ocean*. Cambridge University Press.

TOMCZAK, M. 1988 Island wakes in deep and shallow water. *J. Geophys. Res.* **93** (C5), 5153–5154.

UBEROI, M. S. & FREYMUTH, P. 1970 Turbulent energy balance and spectra of the axisymmetric wake. *Phys. Fluids* **13** (9), 2205–2210.

WAITE, M. L. & BARTELLO, P. 2003 Stratified turbulence dominated by vortical motion. *J. Fluid Mech.* **517**, 281–308.

WINTERS, K. B., MCKINNON, J. & MILLS, B. 2004 A spectral model for process studies of density stratified flows. *J. Atmos. Ocean. Technol.* **21** (1), 69–94.

ZALESAK, S. T. 1979 Fully multidimensional flux-corrected transport algorithms for fluids. *J. Comput. Phys.* **31**, 335–362.